nature electronics

SUPPLEMENTARY INFORMATION

https://doi.org/10.1038/s41928-018-0058-4

In the format provided by the authors and unedited.

Field-effect transistors made from solution-grown two-dimensional tellurene

Yixiu Wang[1,9], Gang Qiu[2,3,9], Ruoxing Wang[1,9], Shouyuan Huang[4], Qingxiao Wang[5], Yuanyue Liu[6,7,8], Yuchen Du[2,3], William A. Goddard III[6], Moon J. Kim[4], Xianfan Xu[3,4], Peide D. Ye[2,3]* and Wenzhuo Wu[1,3]*

[1]School of Industrial Engineering, Purdue University, West Lafayette, IN, USA. [2]School of Electrical and Computer Engineering, Purdue University, West Lafayette, IN, USA. [3]Birck Nanotechnology Center, Purdue University, West Lafayette, IN, USA. [4]School of Mechanical Engineering, Purdue University, West Lafayette, IN, USA. [5]Department of Materials Science and Engineering, University of Texas at Dallas, Richardson, TX, USA. [6]The Resnick Sustainability Institute, California Institute of Technology, Pasadena, CA, USA. [7]Materials and Process Simulation Center, California Institute of Technology, Pasadena, CA, USA. [8]Texas Materials Institute, Department of Mechanical Engineering, The University of Texas at Austin, Austin, TX, USA. [9]These authors contributed equally: Yixiu Wang, Gang Qiu and Ruoxing Wang *e-mail: yep@purdue.edu; wenzhuowu@purdue.edu

1. Supplementary Notes

Supplementary Note 1: Discussion on the temperature effect

The tellurene synthesis is also influenced by the reaction temperature. The reaction was carried out through the reduction of Na_2TeO_3 by hydrazine in alkaline solution. The reaction equation can be written as follow[9]:

$$TeO_3^{2-} + 3H_2O + 4e^- \rightarrow Te + 6OH^- \ \varphi^\theta = -0.57\ V$$

$$N_2H_4 + 4OH^- \rightarrow N_2 \uparrow + 4H_2O + 4e^- \ \varphi^\theta = -1.16\ V$$

where φ^θ is the standard electrode potential. They are measured at 298 K and under standard pressure ($p^\theta = 100kPa$). According to Nernst equation, $\Delta G = -zEF$, where z is the number of transferred electrons, E is the electromotive force, and F is the Faraday constant, which is 96500 C·mol^{-1}, the overall reaction is spontaneous change because of the negative change of Gibbs free energy, which seems not to be related to the temperature. However, the half reaction of hydrazine oxidation is endothermic reactions, driven by the increase of entropy. The higher temperature promotes the forward reaction rate in this half reaction, leading to higher productivity of 2D Te. It can be seen in Supplementary Fig. 8 that the productivity dramatically increased from 160 ℃ to 180 ℃. But there is no significant difference between 180 ℃ and 200 ℃, possibly due to the breaking of the weak van der Waals bonds between Te chains and the damaging the 2D Te nanostructures by the high temperature with extra energy of Te atoms. There may be a balance between the improvement of the degree of reaction and the excessive energy decomposing the nanostructure. These results warrant further in-depth investigations.

Thickness-mobility dependence fitting

The field-effect mobility displays a non-monotonic dependence on Te film thickness. Thomas-Fermi screening effect[10] has been successfully applied to model the total conductance in a biased 2D material film with a certain thickness, such as graphene, MoS_2, and black phosphorus[11-13]. Here we adopted the same method to fit the mobility-thickness relationship. Due to charge screening, the mobility μ and carrier density n in thin films are no longer uniform but a function of the depth from the interface z. Considering a slab with infinitesimal thickness dz at depth z, the total conductance σ(z+dz) will be the conductance of this thin slab plus the total conductance of σ(z) in series with two interlayer resistance R_{int} to form a resistor network as shown in Fig. S15, which gives recursion equation[11]:

$$\sigma(\mathrm{z}+\mathrm{dz}) = \mathrm{qn(z)\mu(z)dz} + \frac{\sigma(\mathrm{z})\frac{1}{2R_{int}}}{\sigma(\mathrm{z})+\frac{1}{2R_{int}}} \quad (1)$$

By replacing R_{int} with the resistance of unit length r multiplied by dz, we can reform the eq. (1) into a differential equation:

$$\frac{d\sigma}{dz} = \mathrm{qn(z)\mu(z)} - \sigma(\mathrm{z})^2\mathrm{r} \quad (2)$$

The Thomas-Fermi screening effect goes that the carrier density and mobility decays as depth increases with a characteristic screening length λ. Therefore we can express n(z) and μ(z) as[12]:

$$\mathrm{n(z)} = \mathrm{n(0)}\exp\left(-\frac{z}{\lambda}\right) \quad (3)$$

$$\mu(\mathrm{z}) = \mu_{inf} - \left(\mu_{inf} - \mu_0\right)\exp(-\frac{z - z_0}{\lambda}) \quad (4)$$

where μ_{inf} and μ_0 are the mobility at infinity and the interface respectively.

By substituting eq.3 and eq.4 back to eq.2, we can derive an expression for total conductance σ(z). Finally, we convert the total conductance into effective mobility with the simple relation:

$$\mu_{FE}(\mathrm{z}) = \frac{\sigma(z)}{Q_{tot}} \quad (5)$$

where Q_{tot} is the total gate-induced charge in the entire channel which can be estimated by multiplying gate voltage by C_{ox}.

This model fits well with our experiment data, and the calculated Thomas-Fermi screen length is 4.8 nm which is a reasonable value compared to other material systems such as MoS_2 and black phosphorus.

Thickness-dependent on/off ratio in 2D Te FETs

Most of the 2D FETs are operated in accumulation-mode or depletion-mode junction-less type field-effect transistors with oxide as the dielectric. Their device operation is very similar to III-V MESFETs or HEMTs and thin film transistors such as Indium–gallium–zinc oxide (IGZO) ones. They are very different from the conventional Si MOSFETs which are operated in inversion-mode and independent on film thickness. A simplified model to demonstrate the degradation of on/off ratio with thickness is presented following. At on-state, the carrier transport is mainly contributed by gate induced accumulated carriers located within a few nanometers from the interface and the doped channel. Therefore, the on-state current varies several times for a wide range of thickness as confirmed by the experimental data. We define the off-state to be the scenario where the Fermi energy is at charge neutral point at the interface, as shown in Figure 1 (for simplicity, we ignore Schottky contact impact and electron and hole mobility difference in off-state). The surface potential or band bending at off-state is deduced to be around 0.15 V, which is a reasonable estimation considering the 0.35 eV bandgap of Te and the fact that the Fermi level of bulk Te is closer to its valence band. Under depletion approximation, we can then derive the surface potential at certain depth x (distance to the interface) by solving Poisson's equation:

$$\varphi_s(x) = \frac{qN_A}{2\varepsilon_s\varepsilon_0}(x - x_d)^2,$$

where ε_s is the permittivity of Te, ε_0 is the vacuum permittivity, N_A is the intrinsic doping level and x_d is the maximum depletion width which is calculated to be

$$x_d = \sqrt{2\varepsilon_s\varepsilon_0\varphi_s(0)/qN_A} \approx 22\ nm,$$

close to experimentally observed thickness range where the on/off ratio starts to saturate. The hole density at x then can be expressed by:

$$p(x) = p_0 \exp(-q\varphi_s(x)/kT).$$

We plotted the surface potential and carrier distribution as a function of distance x in Figure 2. By integrating carrier density $p(x)$ with x, the off-state sheet carrier density can be numerically calculated as a function of flake thickness t:

$$n_{2D\_off}(t) = \int_0^t p(x)dx,$$

as shown in Figure 3. We can see that the off-state carrier sheet density increases by more than 4 orders as the thickness increases from monolayer to over 22 nm. Since

$$I_{on}/I_{off} \approx 1/I_{off} \propto 1/n_{2D\_off}(t),$$

we expect the on/off ratio degrades as carrier density increases in thicker flakes. If the film thickness is larger than the maximum depletion width, the device cannot be turned off, and the situation becomes trivial and obvious.

Noted that the above discussion is barely a simplified illustration why on/off ratio has such a thickness-dependent trend whereas in real devices the situation can be much more complicated.

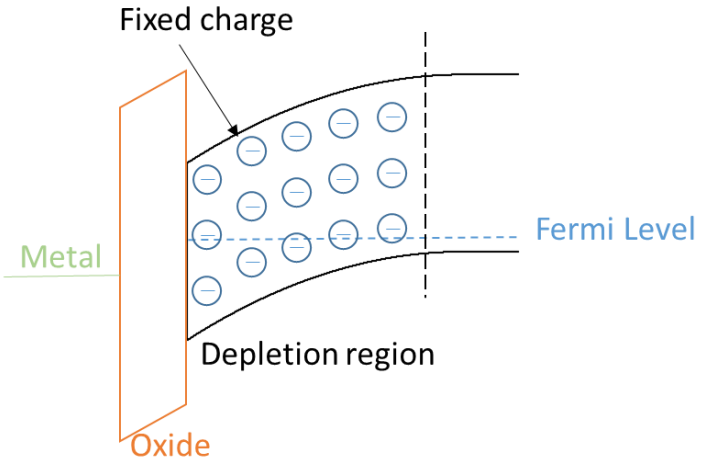

Figure 1. *Band diagram at along MOS stack direction. We define the off-state to be the scenario where the Fermi level at the interface is located at the charge neutral level.*

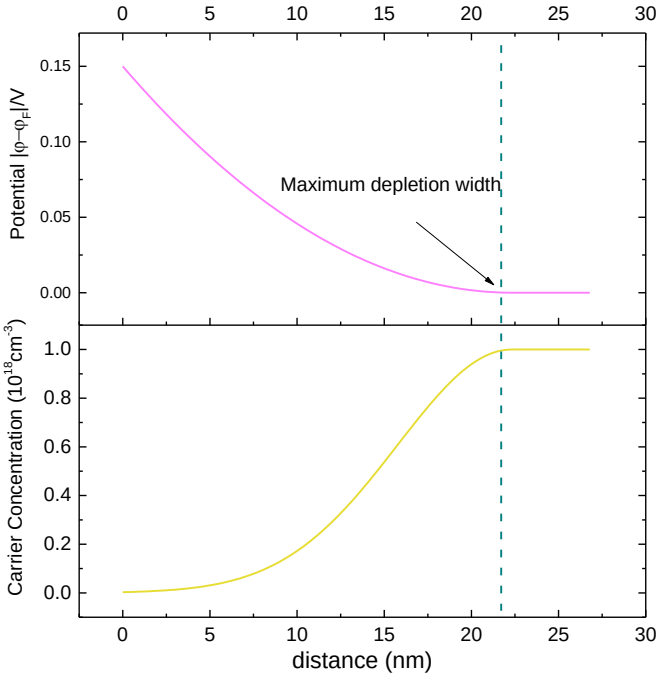

Figure 2. *The potential (upper) and carrier concentration (lower) distribution at off-state as a function of distance from the semiconductor-oxide interface. The maximum depletion width is around 22.3 nm.*

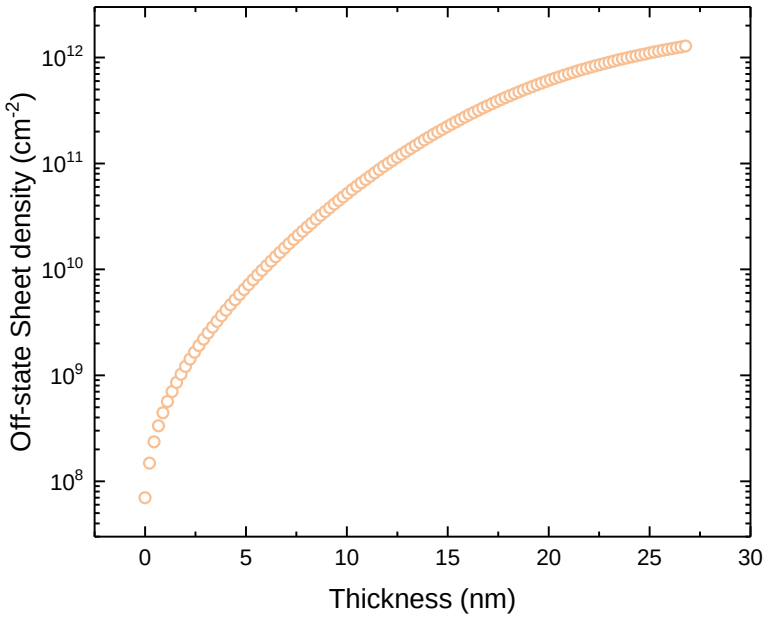

Figure 3. *The 2D sheet density at off-states for flakes with different thickness.*

References:

1 Kresse, G. & Furthmüller, J. Efficient iterative schemes for *ab initio* total-energy calculations using a plane-wave basis set. *Phys. Rev. B* **54**, 11169-11186 (1996).

2 Kresse, G. & Joubert, D. From ultrasoft pseudopotentials to the projector augmented-wave method. *Phys. Rev. B* **59**, 1758-1775 (1999).

3 Blöchl, P. E. Projector augmented-wave method. *Phys. Rev. B* **50**, 17953-17979 (1994).

4 Monkhorst, H. J. & Pack, J. D. Special points for Brillouin-zone integrations. *Phys. Rev. B* **13**, 5188-5192 (1976).

5 Perdew, J. P., Burke, K. & Ernzerhof, M. Generalized Gradient Approximation Made Simple. *Phys. Rev. Lett.* **77**, 3865-3868 (1996).

6 Paier, J. *et al.* Screened hybrid density functionals applied to solids. *J. Chem. Phys.* **124**, 154709, (2006).

7 Zhu, Z. *et al.* Tellurene-a monolayer of tellurium from first-principles prediction. doi:arXiv:1605.03253 (2016).

8 Pine, A. S. & Dresselhaus, G. Raman Spectra and Lattice Dynamics of Tellurium. *Physical Review B* **4**, 356-371 (1971).

9 Liu, Z. *et al.* Shape-controlled synthesis and growth mechanism of one-dimensional nanostructures of trigonal tellurium. *New Journal of Chemistry* **27**, 1748-1752, (2003).

10 Resta, R. Thomas-Fermi dielectric screening in semiconductors. *Physical Review B* **16**, 2717-2722 (1977).

11 Li, L. *et al.* Black phosphorus field-effect transistors. *Nat Nano* **9**, 372-377, (2014).

12 Sui, Y. & Appenzeller, J. Screening and Interlayer Coupling in Multilayer Graphene Field-Effect Transistors. *Nano Letters* **9**, 2973-2977, (2009).

13 Das, S. & Appenzeller, J. Screening and interlayer coupling in multilayer MoS_2. *Physica status solidi (RRL) – Rapid Research Letters* **7**, 268-273, (2013).

Supplementary Figures

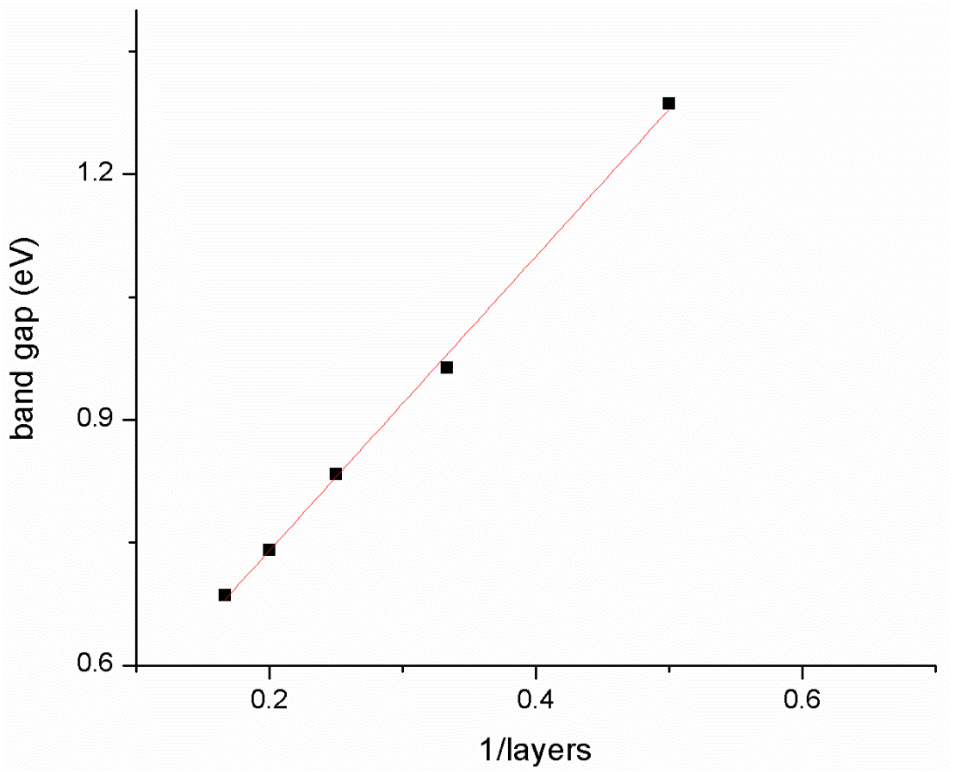

Supplementary Figure 1 | Thickness-dependent bandgap for tellurene, calculated by HSE functional. The bandgap shows a linear dependence on the inverse number of layers, following $E_g = 0.38 + 1.8/n$ (eV). As n goes to infinity, this relation gives a band gap of 0.38 eV for the bulk Te, in good agreement with the experimental data. Given the interlayer distance ~ 3.91 Å, this relation can be rewritten as $E_g = 0.38 + 1.8*3.91/t$ (eV), where t is the thickness (Å).

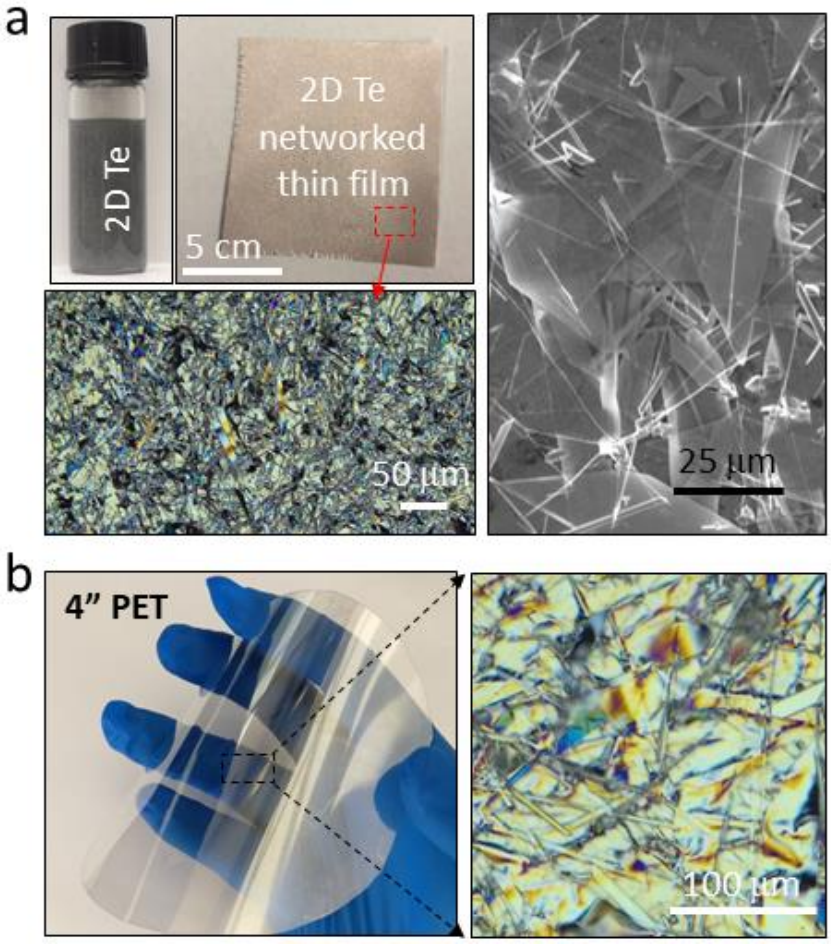

Supplementary Figure 2 | Large-scale transfer and assembly of 2D tellurene into **(a)** networked thin film through ink-jet printing and **(b)** monolayer thin film through LB method.

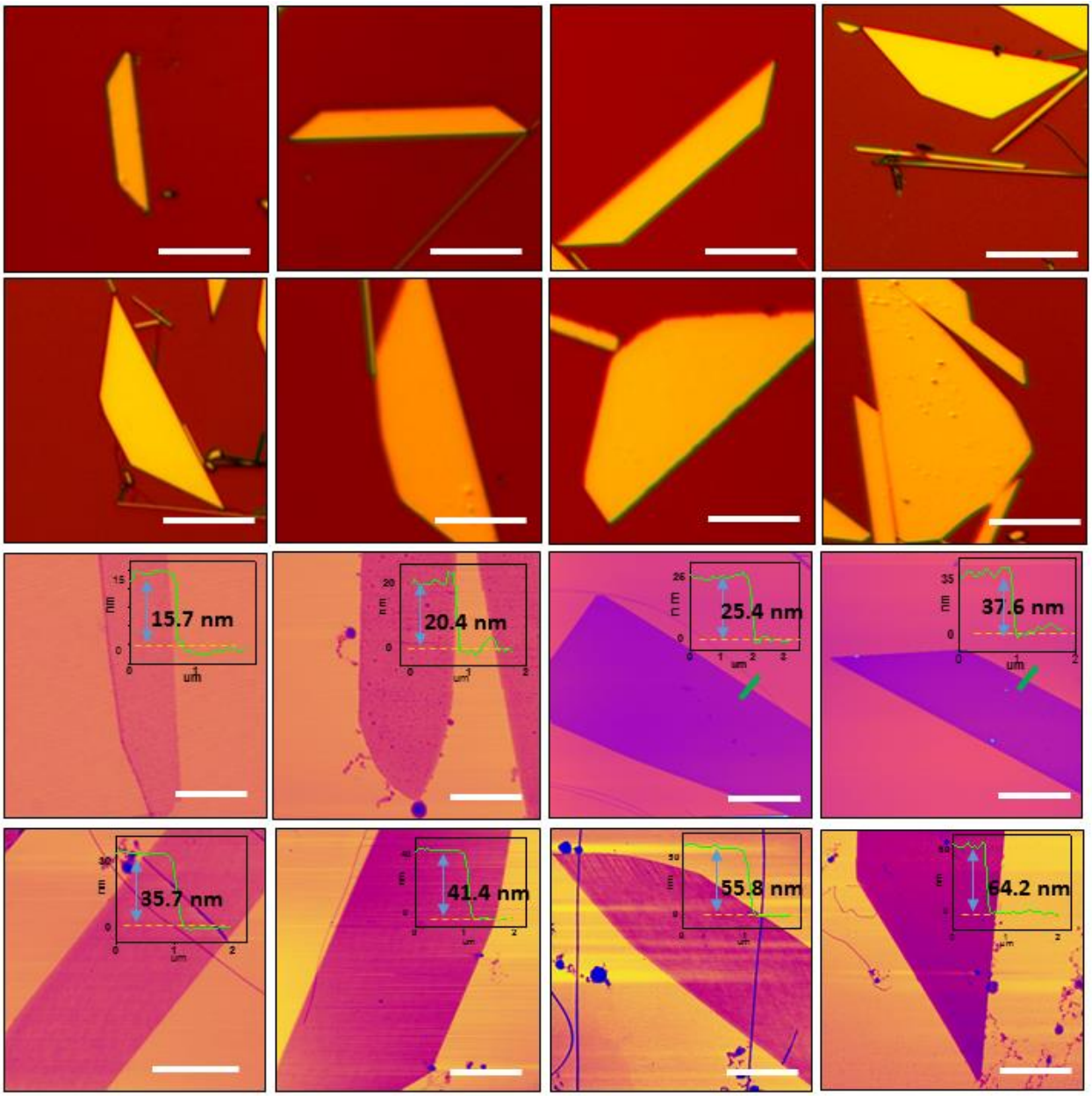

Supplementary Figure 3 | Optical and AFM images of tellurene flakes with various edge lengths and thicknesses. The scale bar is 20 μm.

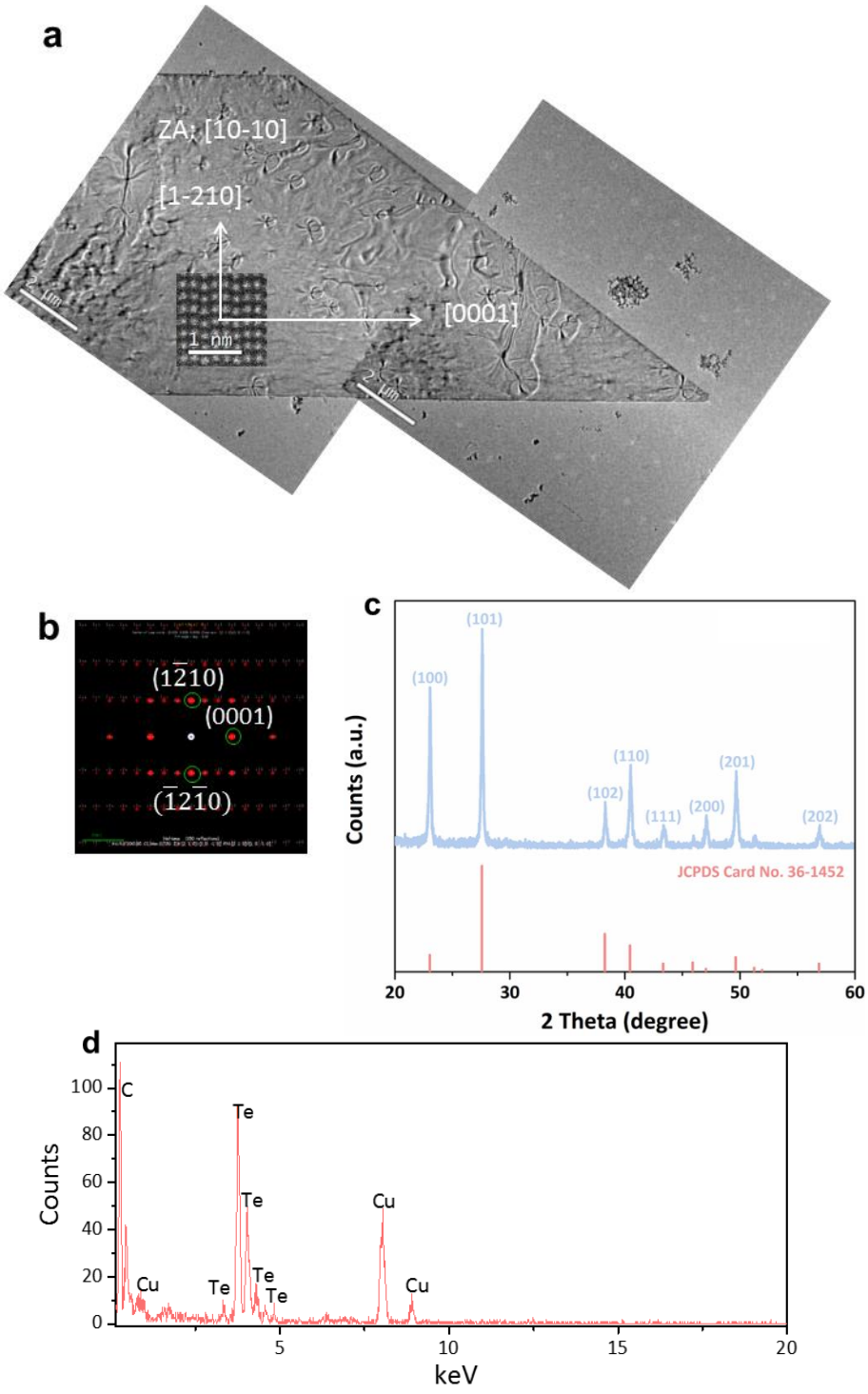

Supplementary Figure 4 | Structural, composition, and quality characterization of tellurene. **a,** Low-resolution TEM image of a tellurene flake. The contour contrast is due to bending of the flake. **b,** Simulated diffraction pattern. **c,** XRD result of 2D Te crystals show high crystallization without impurity peaks in the material, in good agreement with JCPDF card number:36-1452 for tellurium. **d,** EDS spectra confirming the chemical composition of Te. The Cu peaks in EDS spectra come from Cu TEM grid.

Time (hrs) / Na_2TeO_3/ PVP	1.5	2	3	5	7
261.8	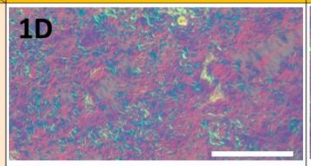	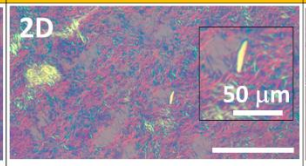	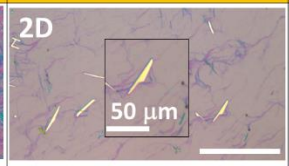	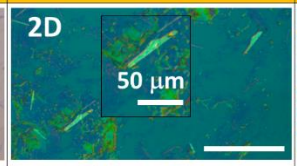	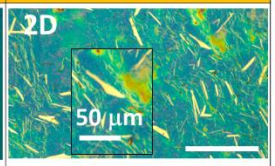
87.3	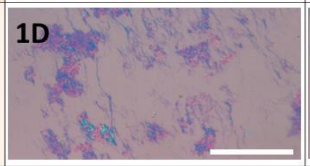	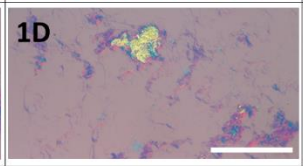	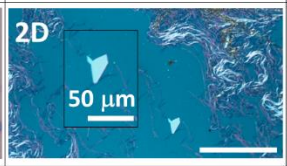	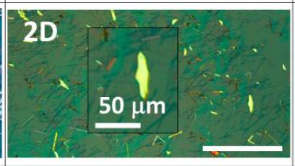	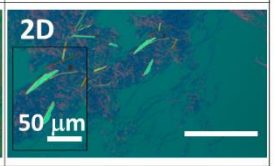
52.4	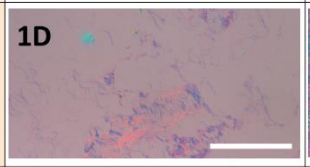	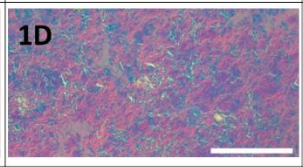	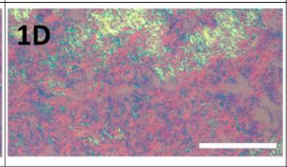	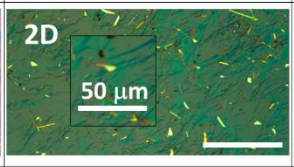	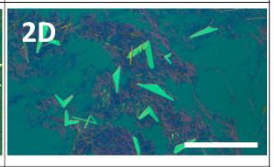
37.4	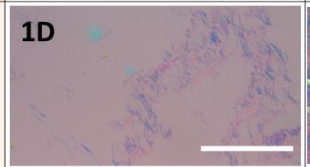	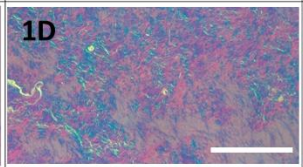	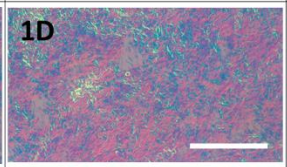	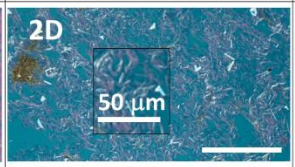	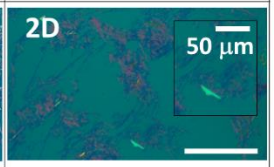
29.1	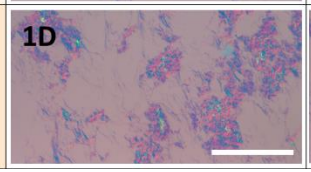	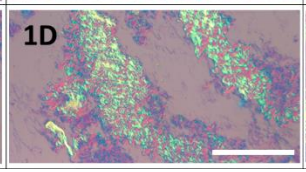	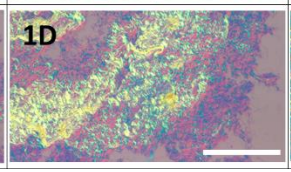	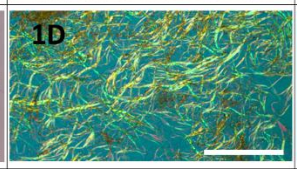	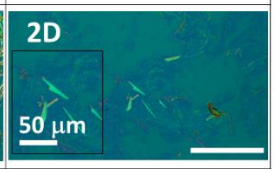

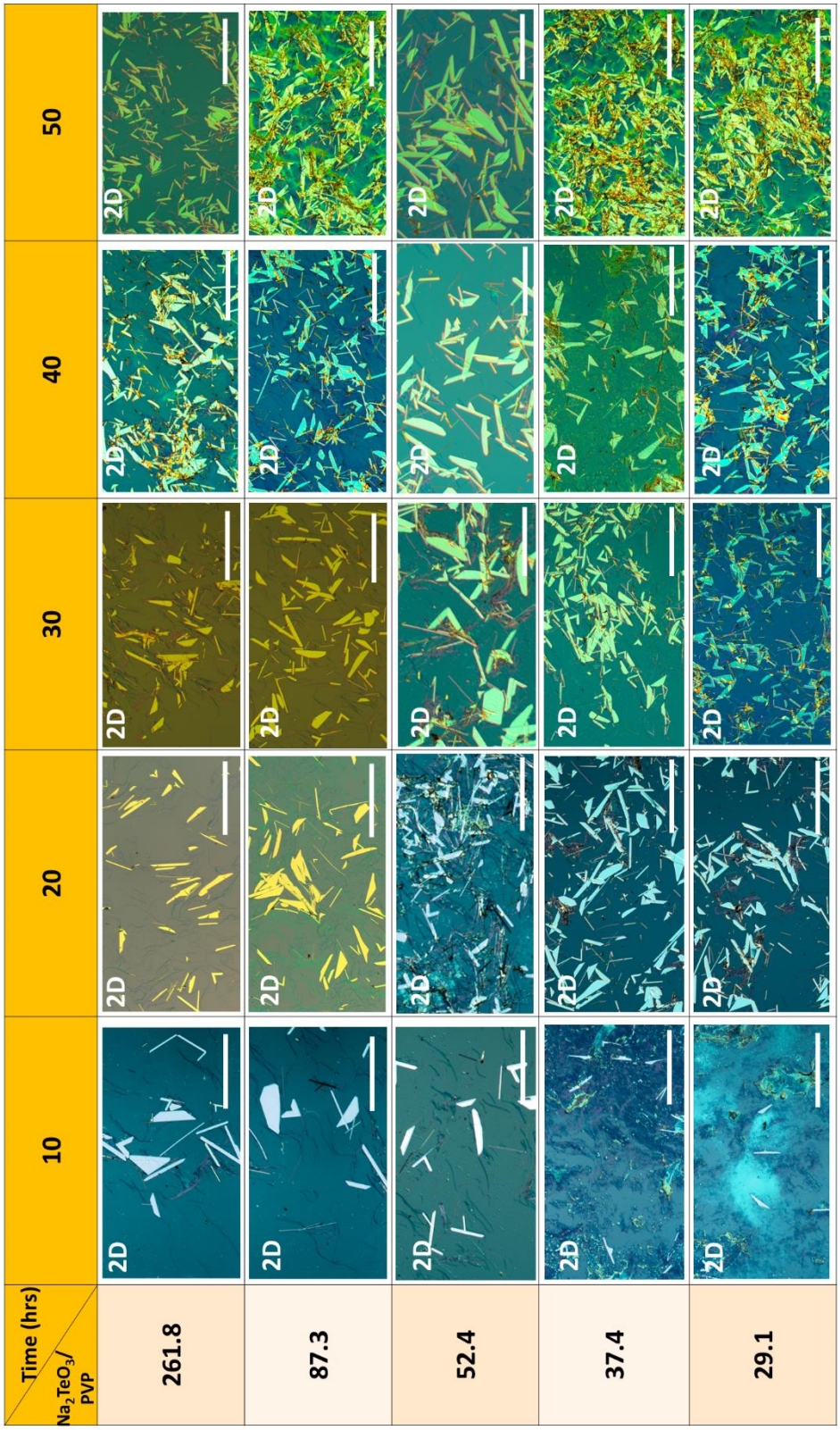

Supplementary Figure 5 | **Morphology evolution in the growth from early to final stages.** The scale bars are 200 μm and 50 μm in the main figures and insets.

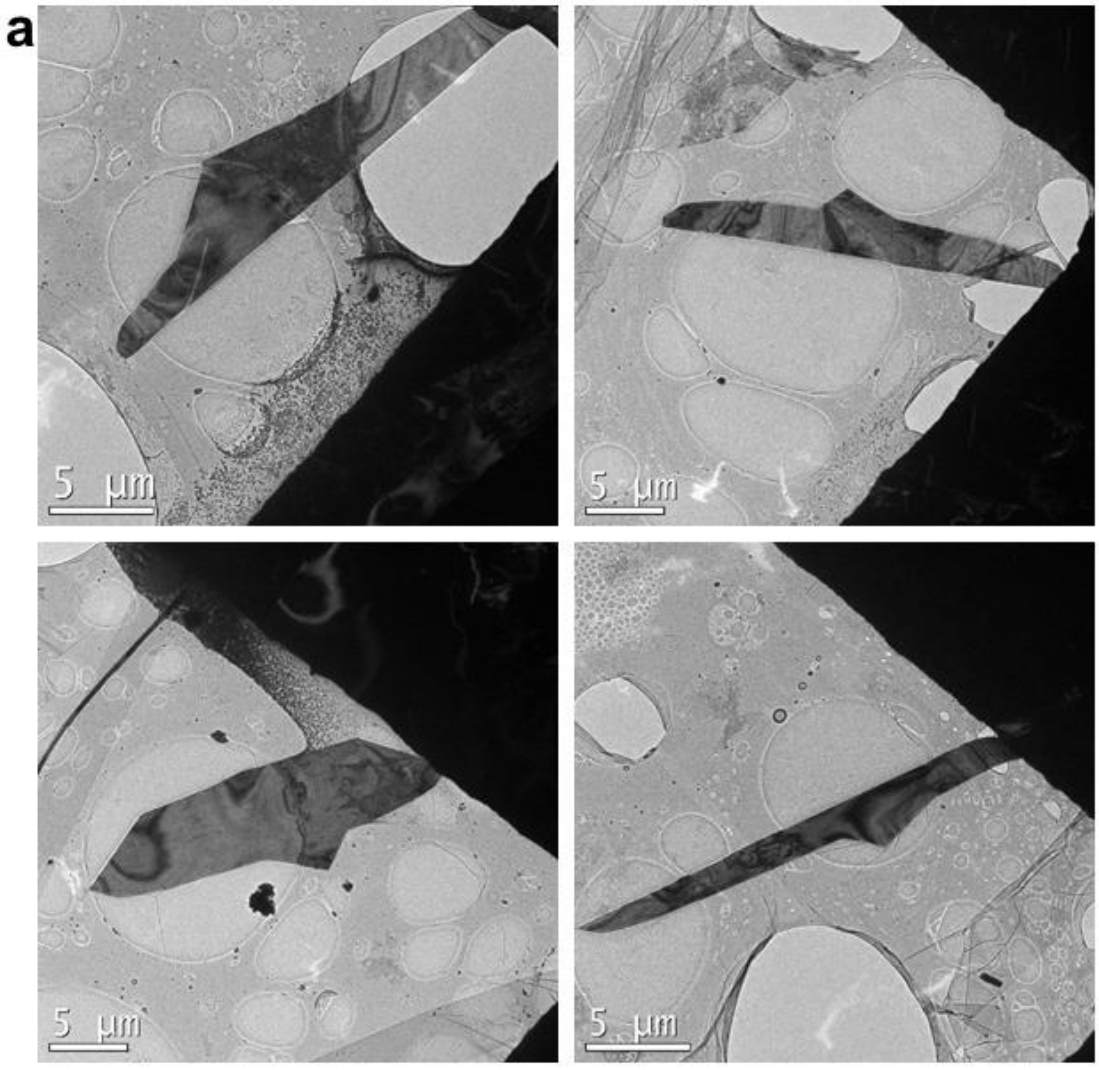
a
5 µm
5 µm
5 µm
5 µm

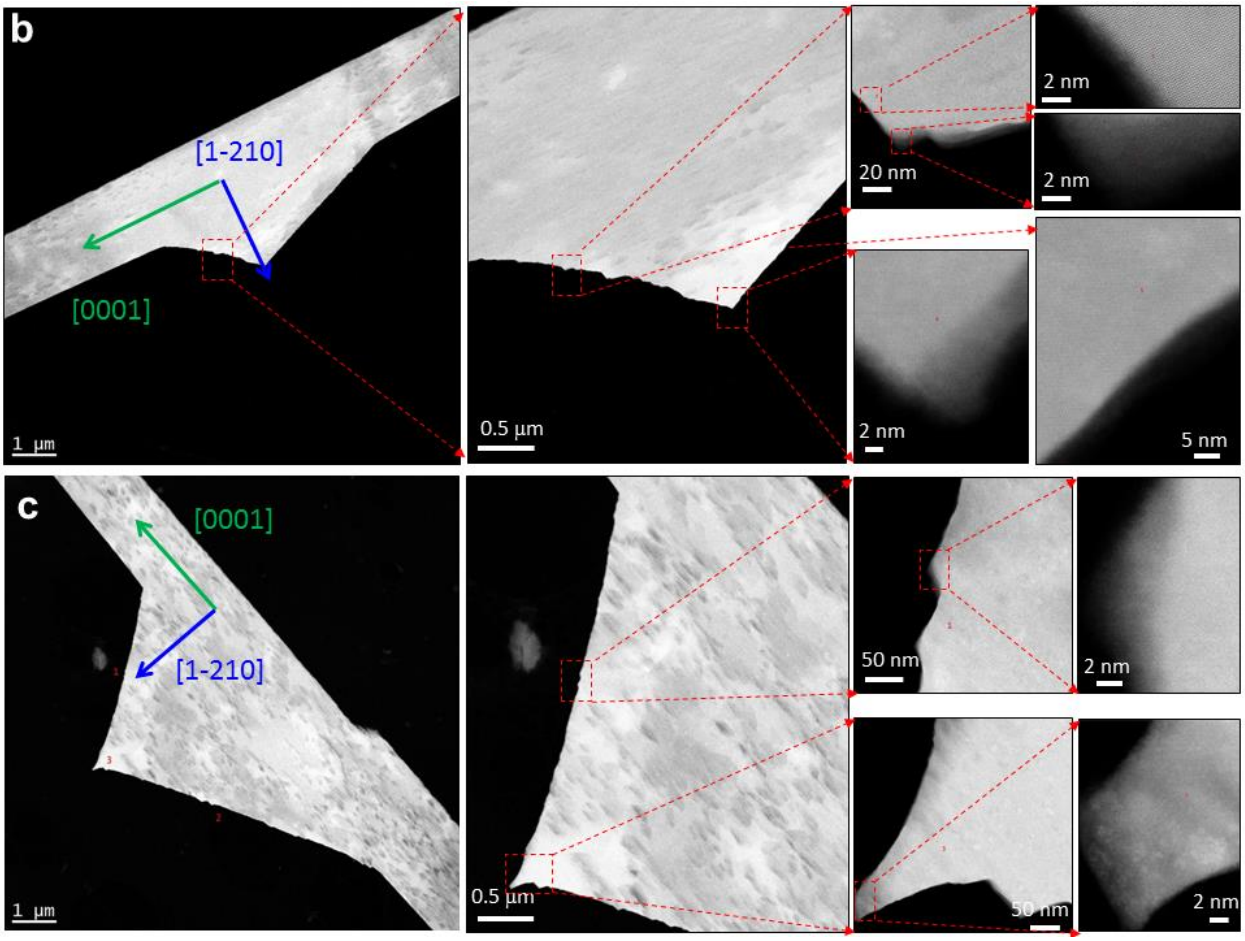

Supplementary Figure 6 | **a,** Low-resolution TEM images of the intermediate structures with edges showing different angles with respect to [0001] direction. **b** and **c**, STEM images of two such structures showing that the edges are made of many steps.

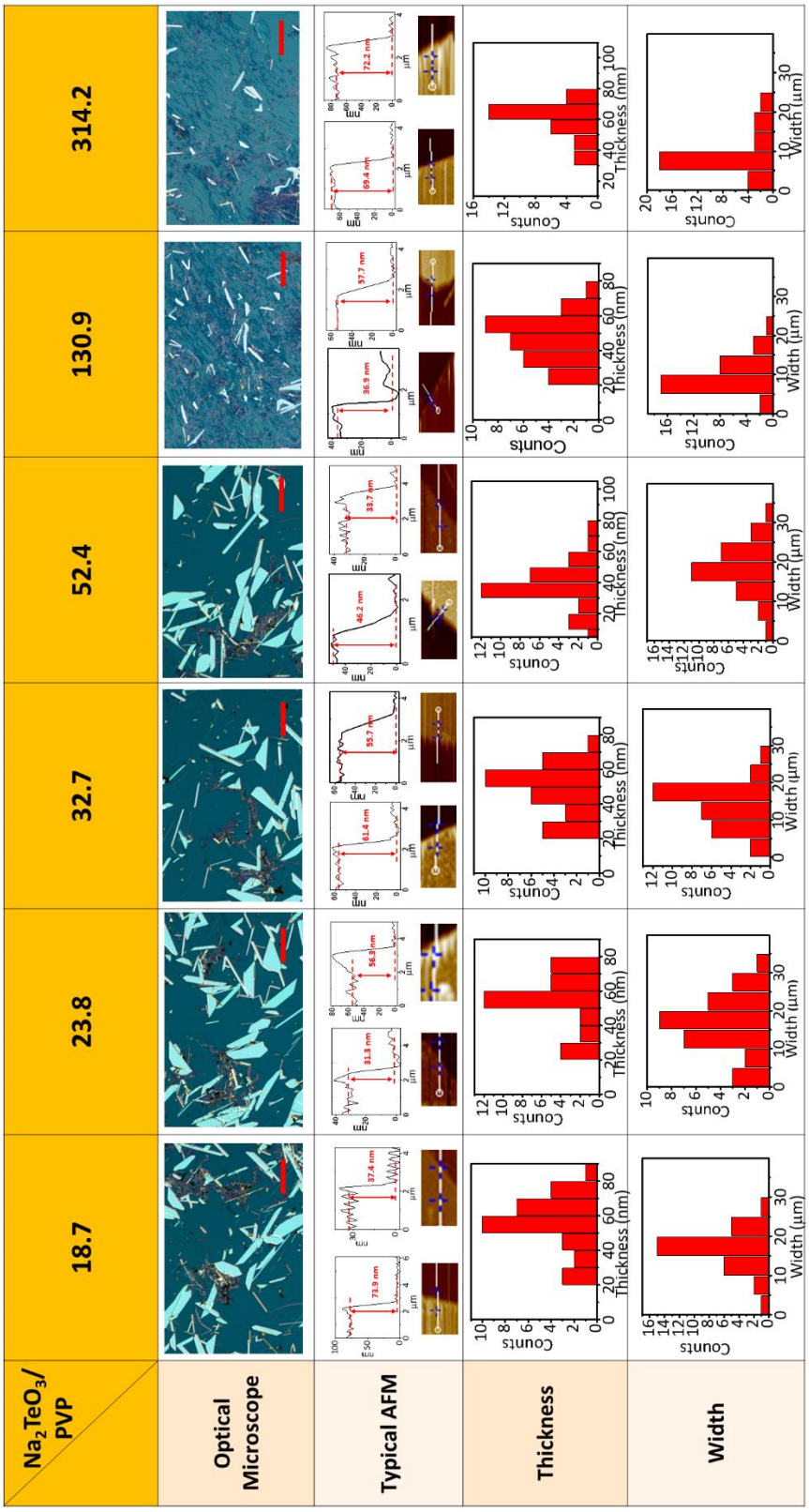

Group	Na_2TeO_3/PVP
1	16.4
2	17.5
3	18.7
4	20.1
5	21.8
6	23.8
7	26.2
8	29.1
9	32.7
10	37.4
11	43.6
12	52.4
13	65.5
14	87.3
15	130.9
16	261.8
17	288.0
18	314.2
19	340.3

Supplementary Figure 7 | AFM data supporting Fig. 2c thickness. The width is the direction which is vertical to <0001>.The scale bar is 50 μm. The table shows the detailed PVP concentration for each group in Fig. 2c.

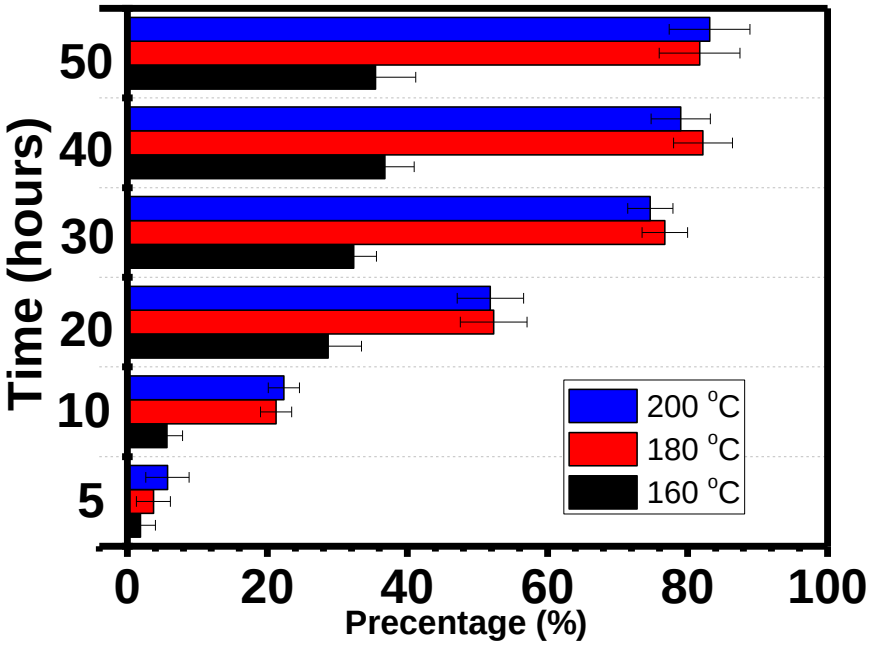

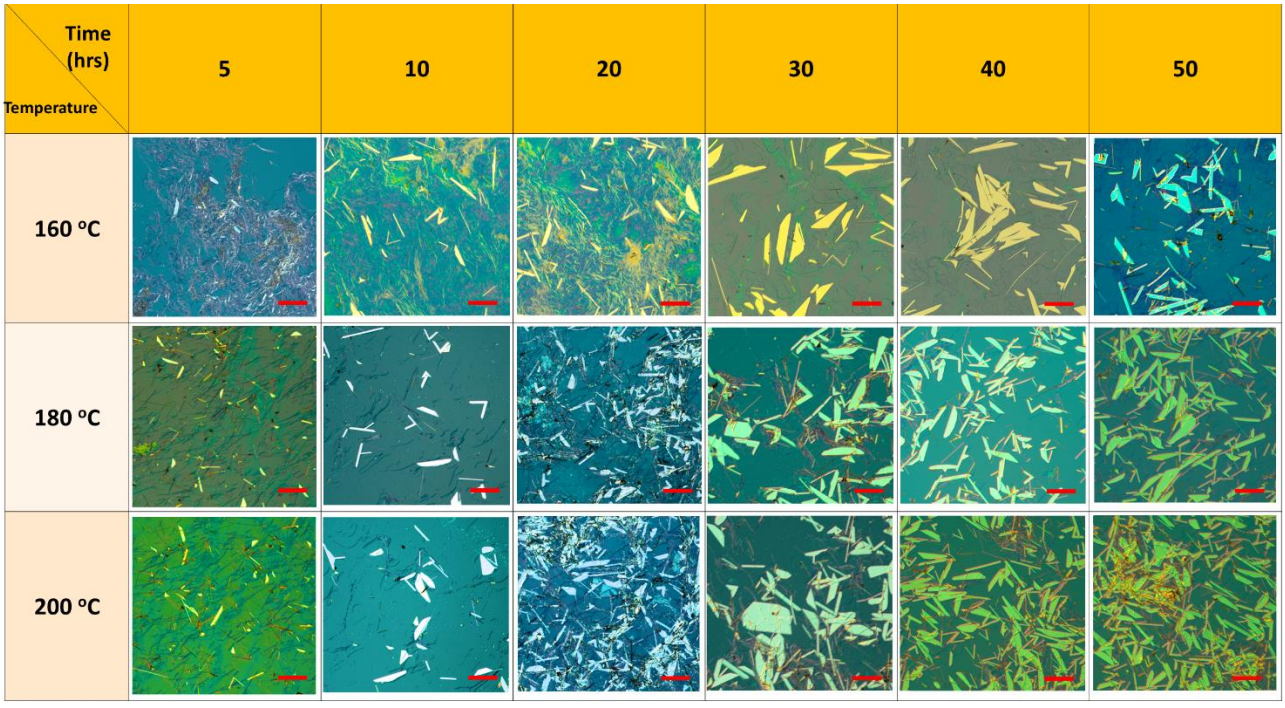

Supplementary Figure 8 | Productivity of tellurene grown at different reaction temperatures. The Na_2TeO_3/PVP ratio is 52.4/1 for all reactions here. Scale bar: 50 μm. Mean values from 5 technical replicates are indicated. Error bars represent s.d.

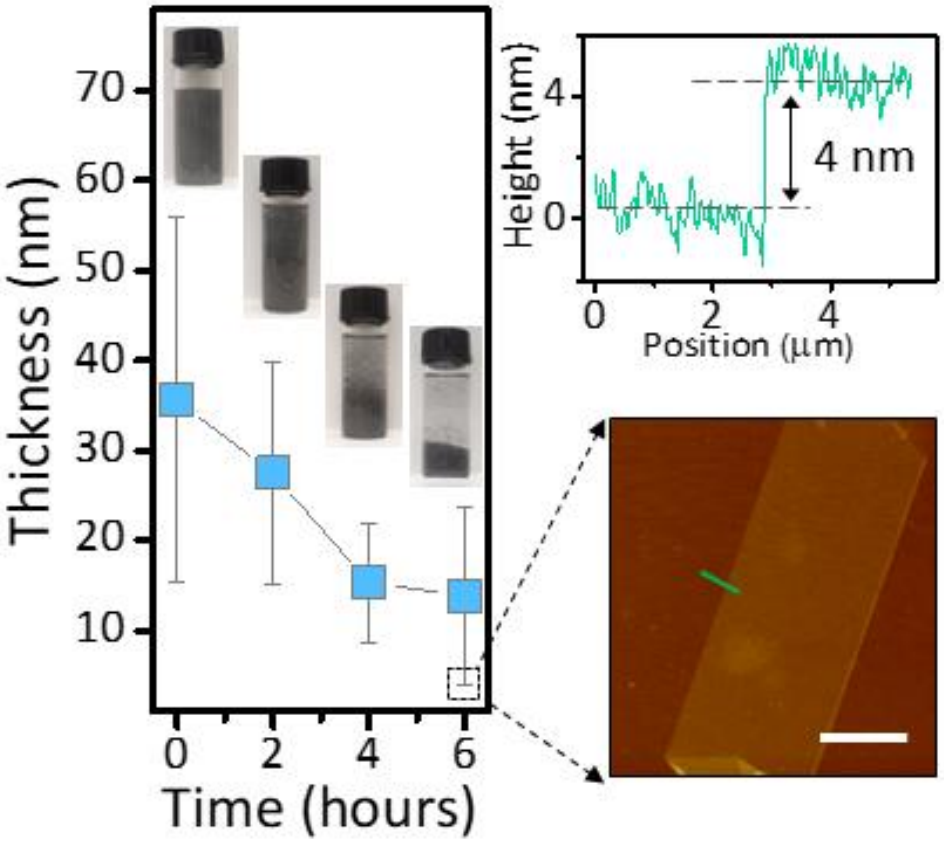

Supplementary Figure 9 | Post-growth thinning process in the alkaline growth solution (pH ~ 11.5) for obtaining ultrathin few-layer tellurene. The scale bar is 5 μm. Mean values from 8 technical replicates are indicated. Error bars represent s.d.

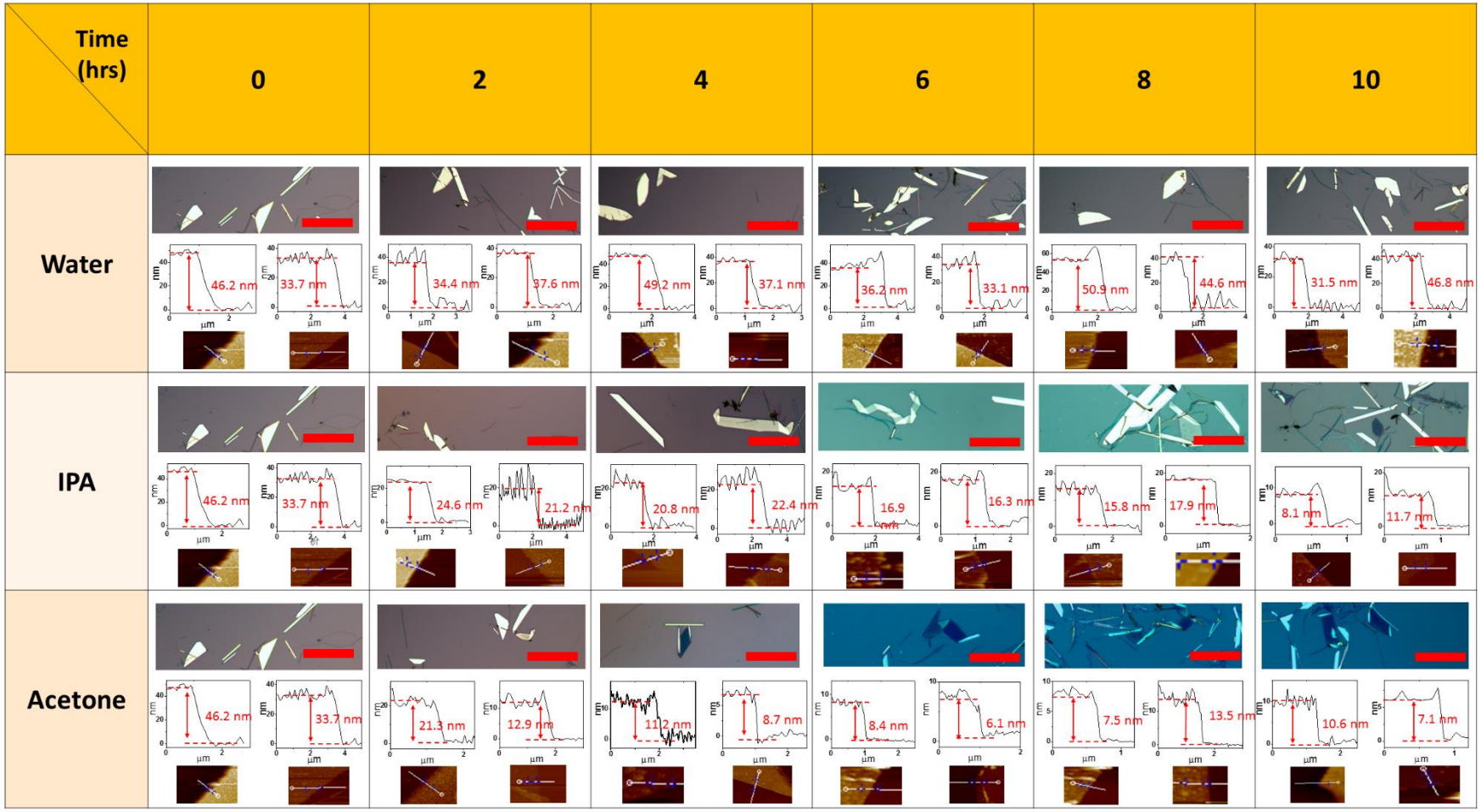
Time (hrs)
0
2
4
6
8
10
Water
46.2 nm
33.7 nm
34.4 nm
37.6 nm
49.2 nm
37.1 nm
36.2 nm
33.1 nm
50.9 nm
44.6 nm
31.5 nm
46.8 nm
IPA
46.2 nm
33.7 nm
24.6 nm
21.2 nm
20.8 nm
22.4 nm
16.9
16.3 nm
15.8 nm
17.9 nm
8.1 nm
11.7 nm
Acetone
46.2 nm
33.7 nm
21.3 nm
12.9 nm
11.2 nm
8.7 nm
8.4 nm
6.1 nm
7.5 nm
13.5 nm
10.6 nm
7.1 nm

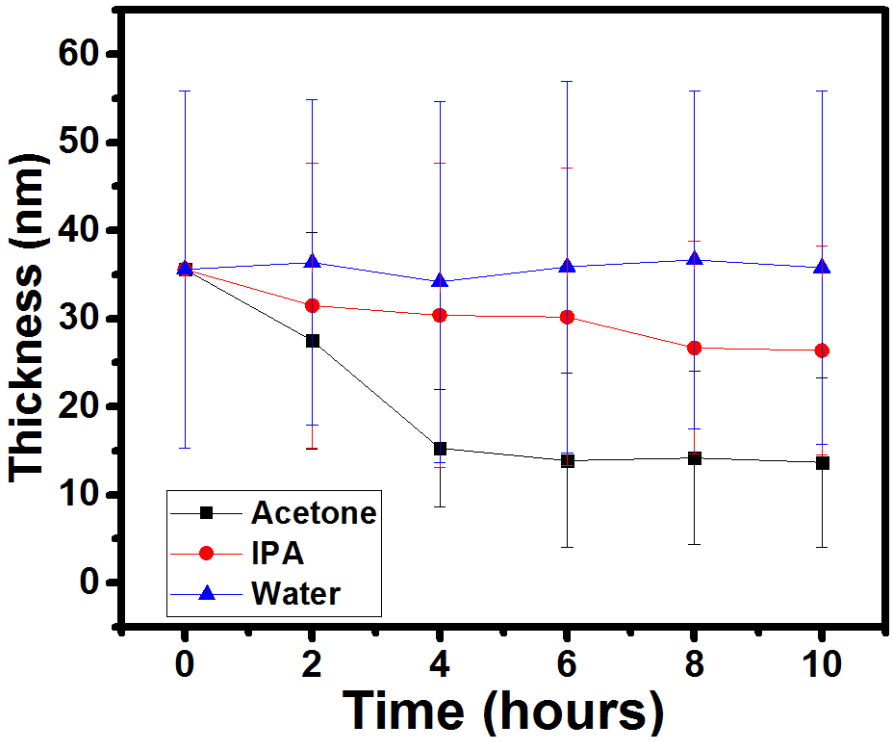

Supplementary Figure 10 | Effect of different solvents on the post-growth thinning of tellurene in the alkaline growth solution (pH ~ 11.5). The scale bar is 50 μm. Mean values from 8 technical replicates are indicated. Error bars represent s.d.

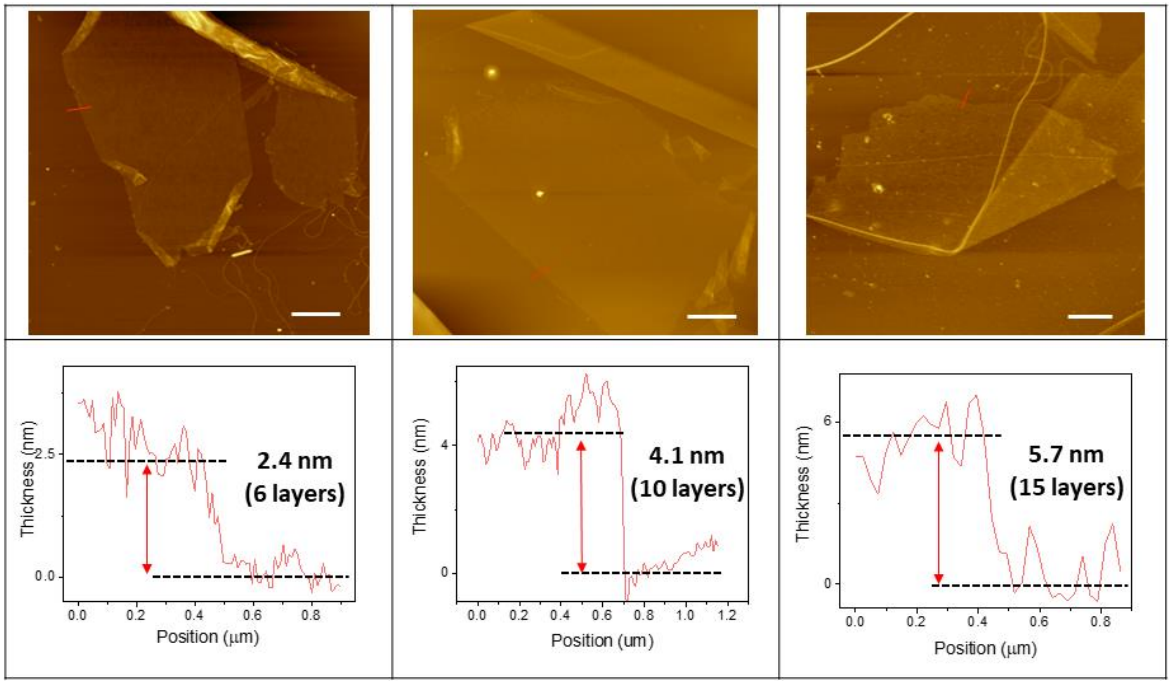

Supplementary Figure 11 | Few-layer tellurene samples obtained after the post-growth thinning process (pH = 10.5) The scale bar is 5 μm.

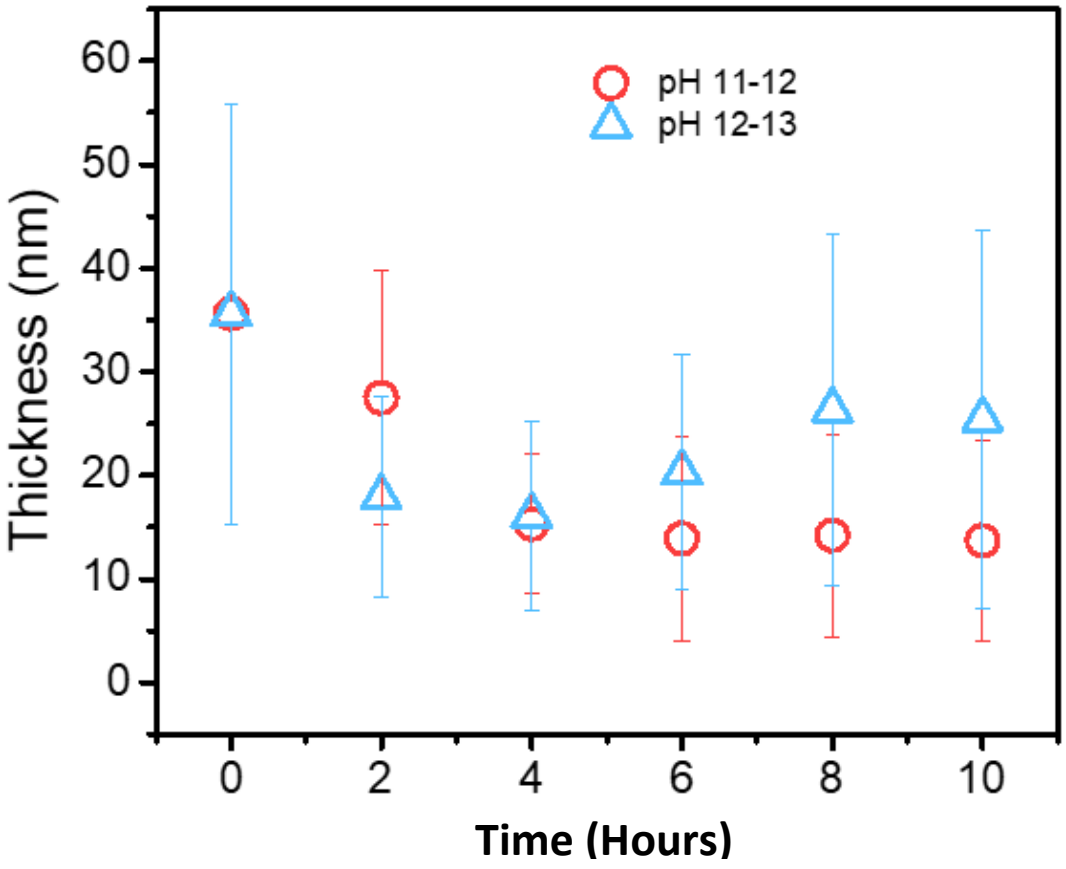

Supplementary Figure 12 | Effect of pH values of the tellurene dispersion solution on the post-growth thinning processes. Mean values from 8 technical replicates are indicated. Error bars represent s.d.

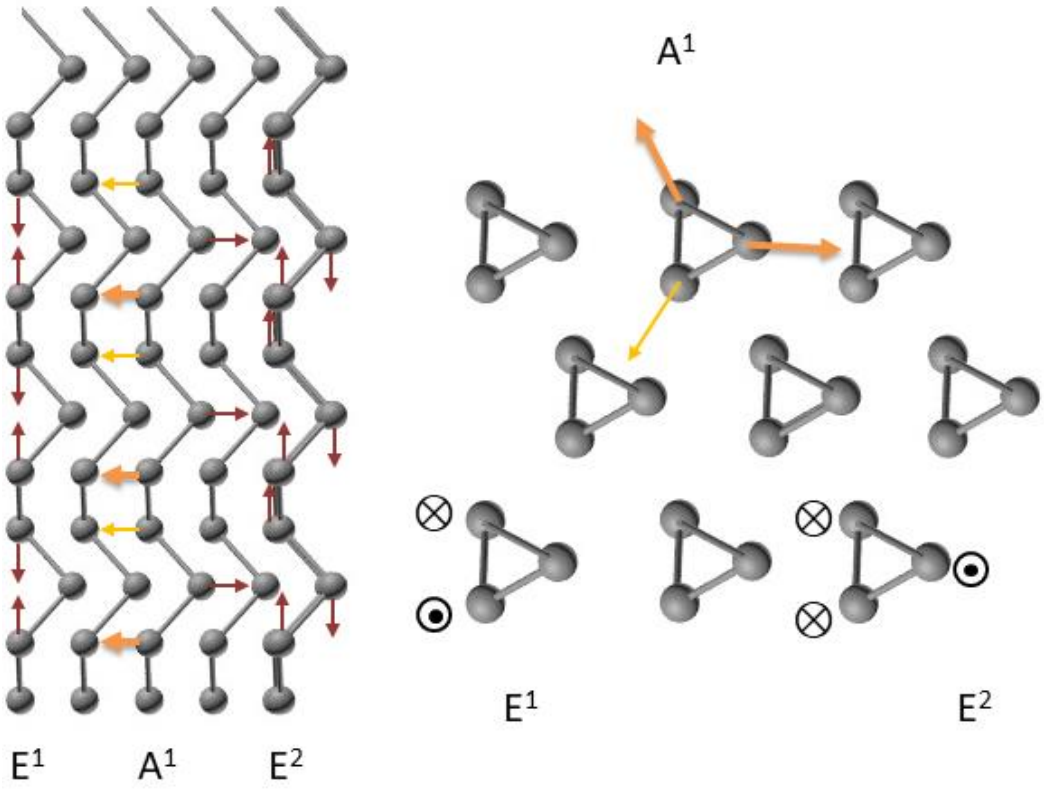

Supplementary Figure 13 | Schematic shows the three main Raman-active modes in chiral-chain van der Waals material tellurene.

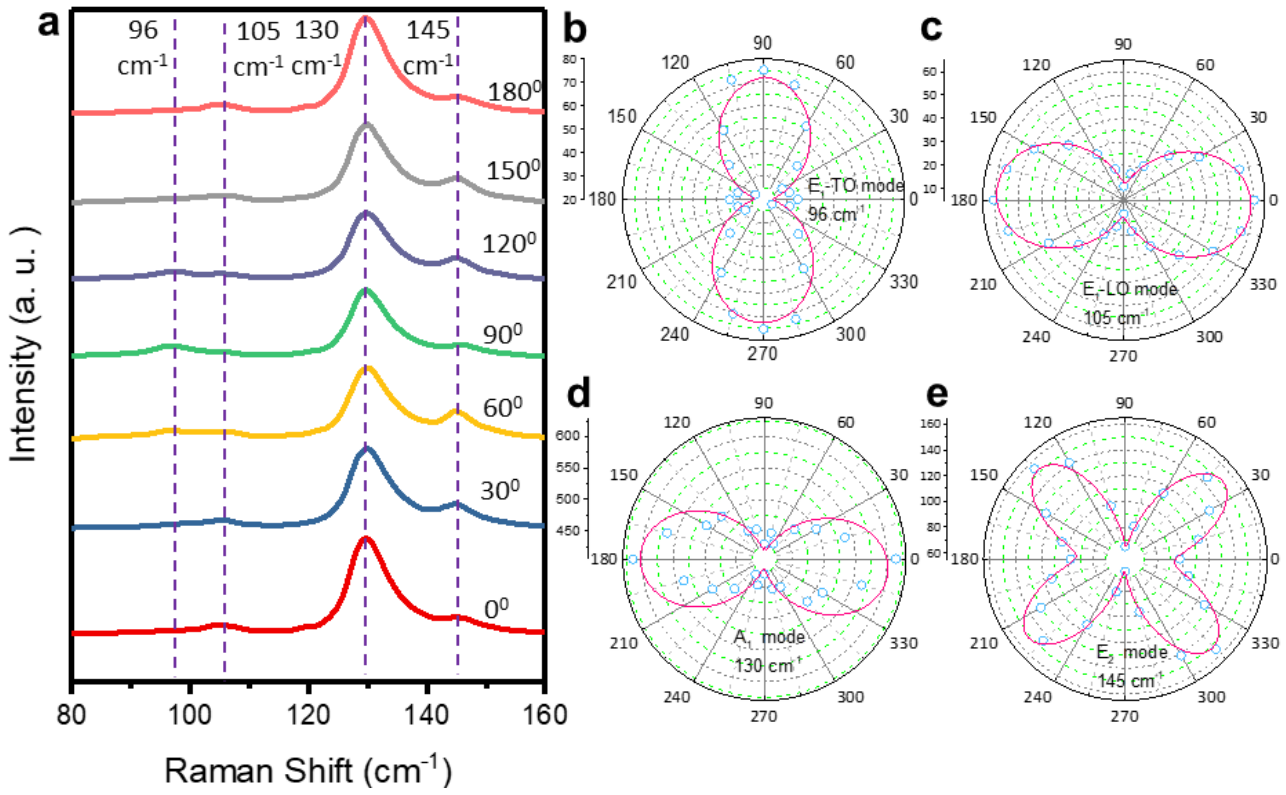

Supplementary Figure 14 | **Angle-resolved Raman Spectra for a 9.7 nm thick sample. a,** Raman spectra evolution with angles between crystal orientation and incident laser polarization. **b-e,** Polar figures of Raman Intensity corresponding to A_1 and two E modes located at 96 (E_1-TO), 105 (E_1-LO), 130 (A_1), and 145 (E_2) cm^{-1}. The fitting curves are described in Supplementary methods.

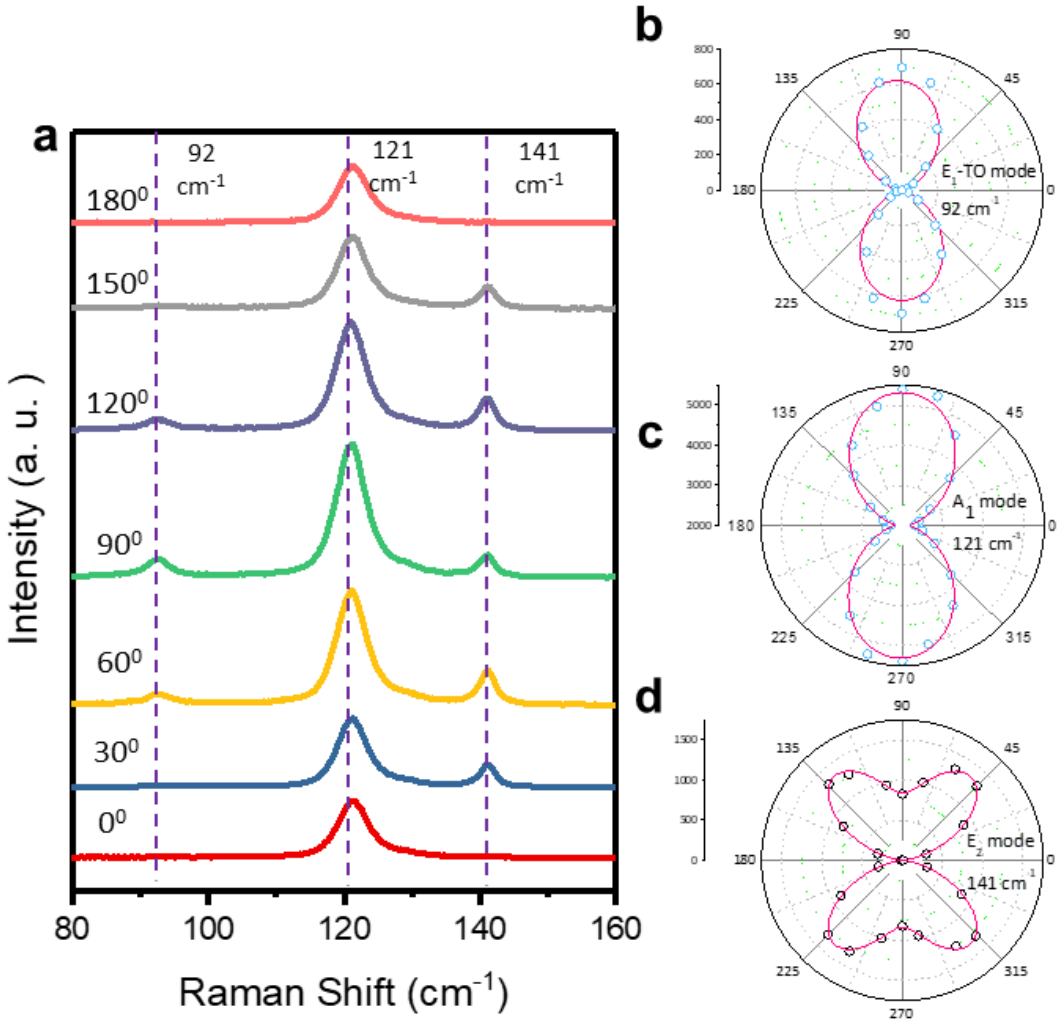

Supplementary Figure 15 | **Angle-resolved Raman Spectra for a 28.5 nm thick sample. a,** Raman spectra evolution with angles between crystal orientation and incident laser polarization. **b-d,** Polar figures of Raman Intensity corresponding to A_1 and two E modes located at 92 (E_1-TO), 121 (A_1), 141 (E_2) cm^{-1}. The fitting curves are described in Supplementary methods.

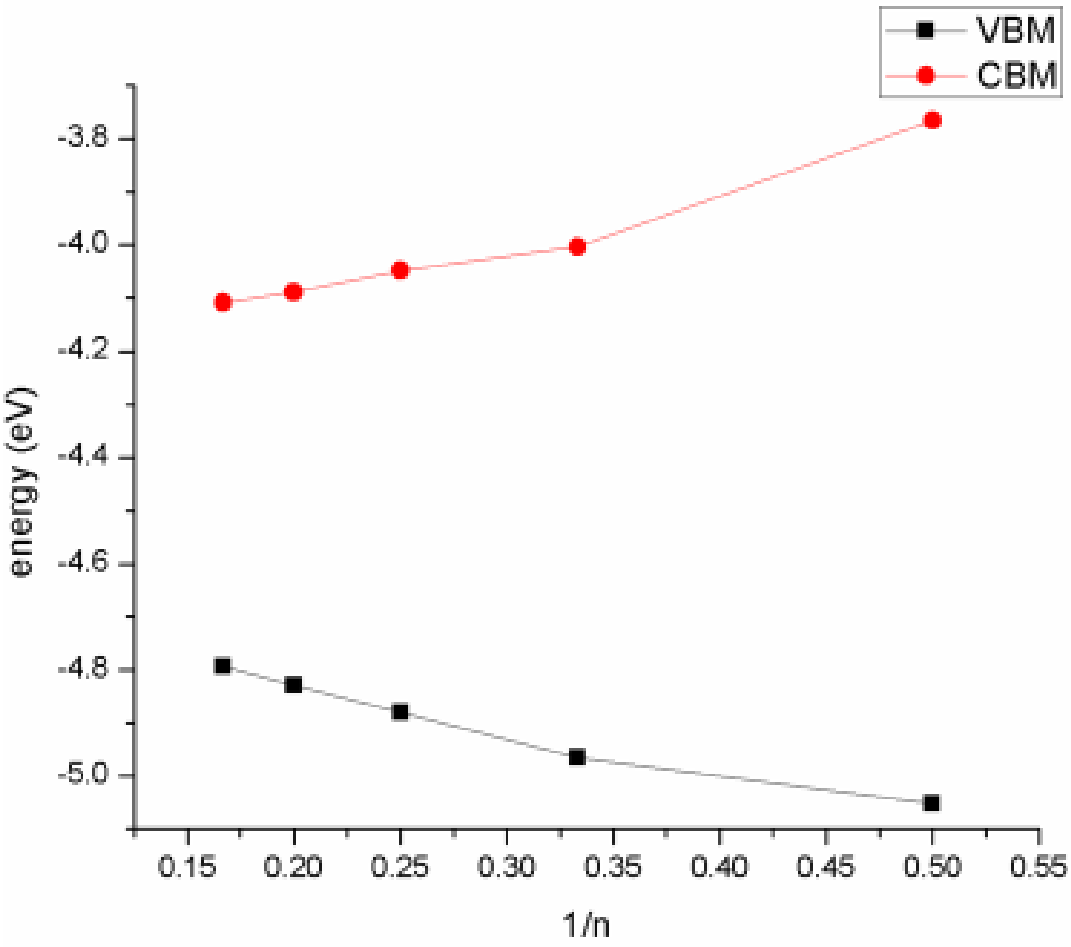

Supplementary Figure 16 | Band edge level (with respect to vacuum) dependence on the number of tellurene layers, calculated by using HSE functional. In experiments, the thickness is > 6 layers. Therefore, the VBM should be at least higher than -4.8 eV. The Pd metal (used as a contact) has a work function of 5.22 - 5.60 eV, below the VBM of Te, so the Te shows a p-type behavior.

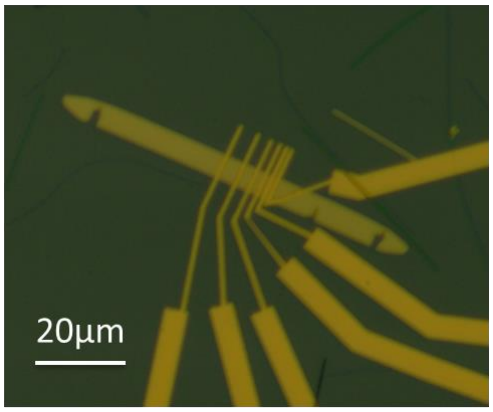

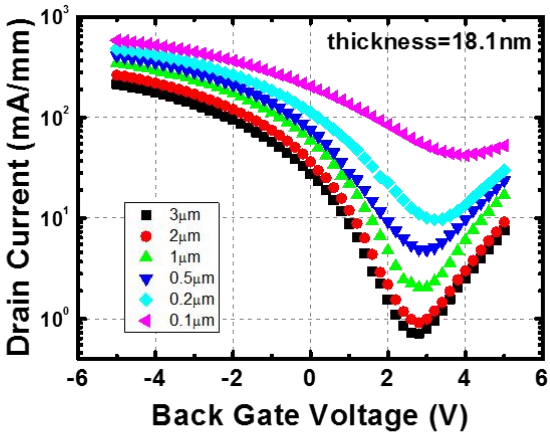

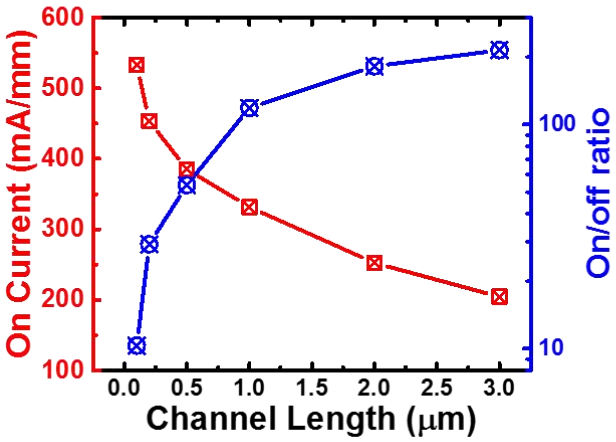

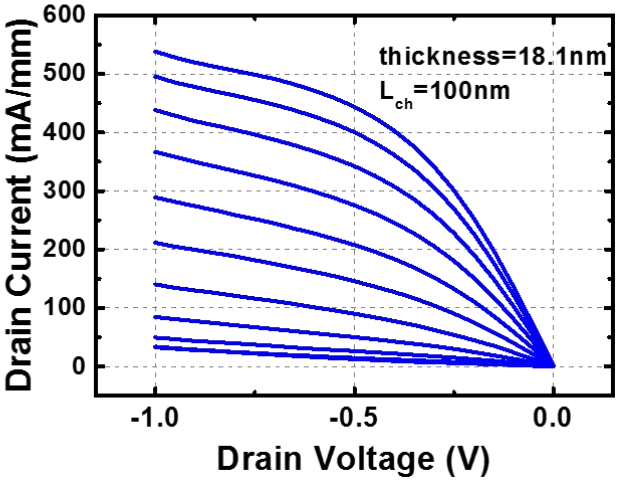

Supplementary Figure 17 | By simply scaling down the channel length to 100 nm, the maximum on-current exceeds 550 mA/mm.

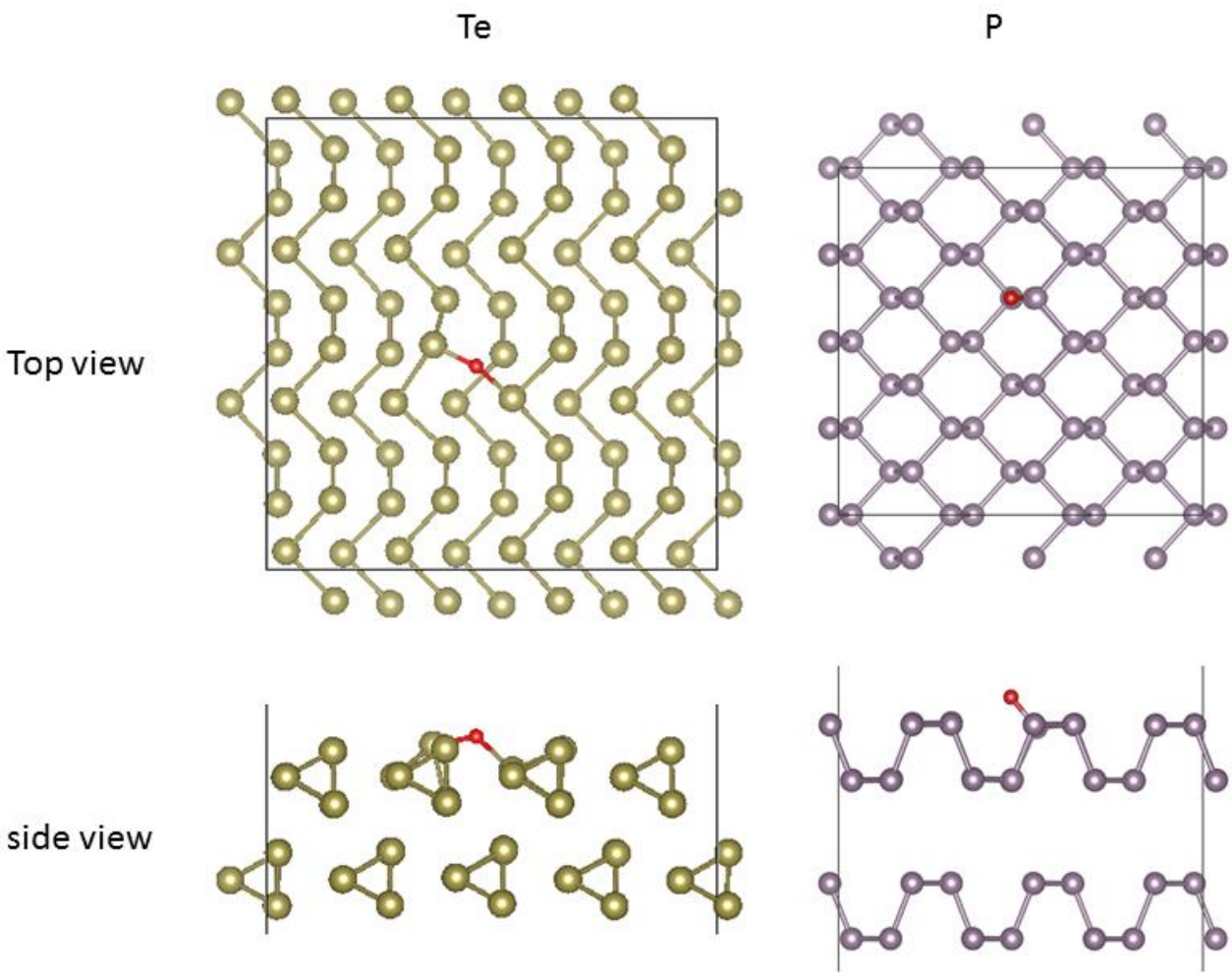

Supplementary Figure 18 | Atomic structure of O adsorption on bilayer Te (left) and P (right). The black lines show the periodic boundaries. Note that the scale bars for Te and P are different. Compared with the binding in O_2, O atom binding to the surface is more favorable by ~-0.7 eV for bilayer Te, while ~ -2 eVs for bilayer P. This explains the superior stability of Te than black P.

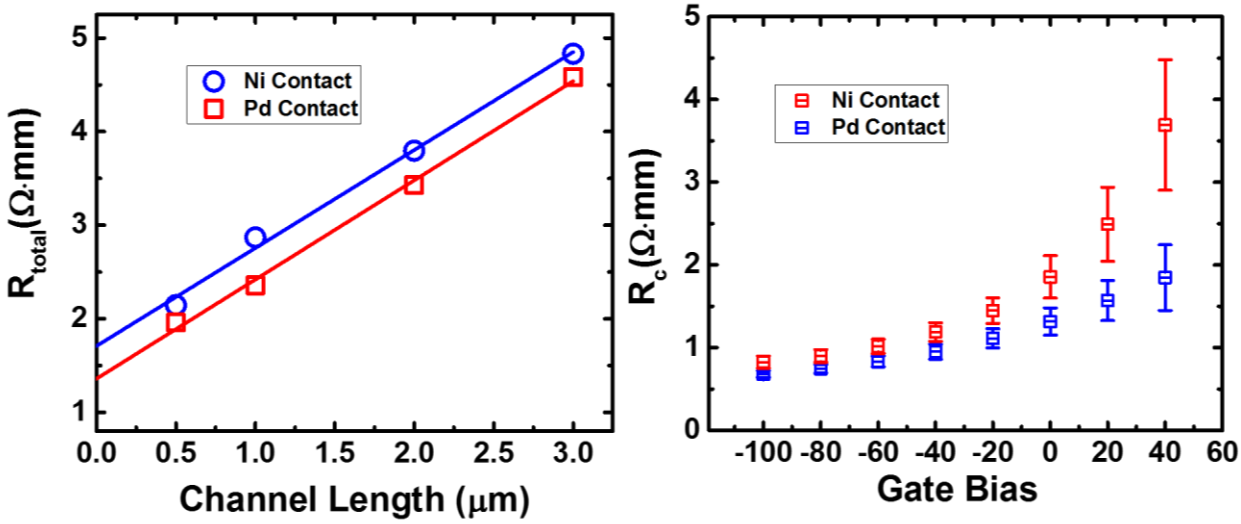

Supplementary Figure 19 | Contact resistance was extracted by transfer length method. By extrapolating linear curve of total resistance vs. channel length, the contact resistance is extracted to be 0.67 and 0.82 Ω·mm on the same flake for Pd and Ni contacts respectively. Error bars arise from a standard error of linear fitting.

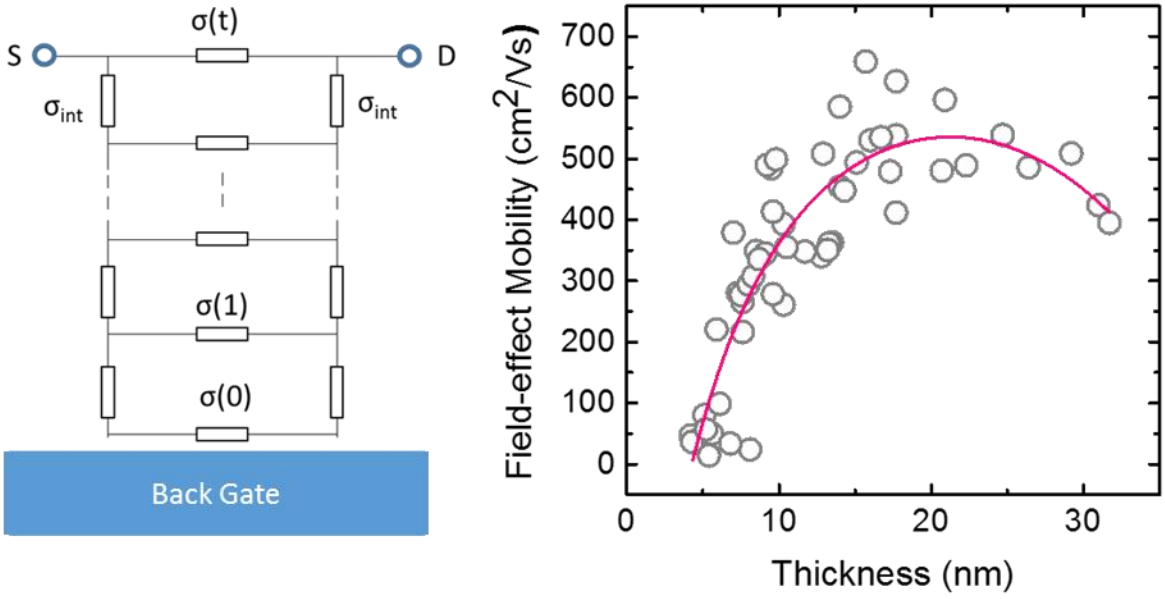

Supplementary Figure 20 | **Left,** the equivalent resistor network model describing total resistance with non-uniform conductance as a function of depth. **Right,** the fitting curve based on the Thomas-Fermi screening model.

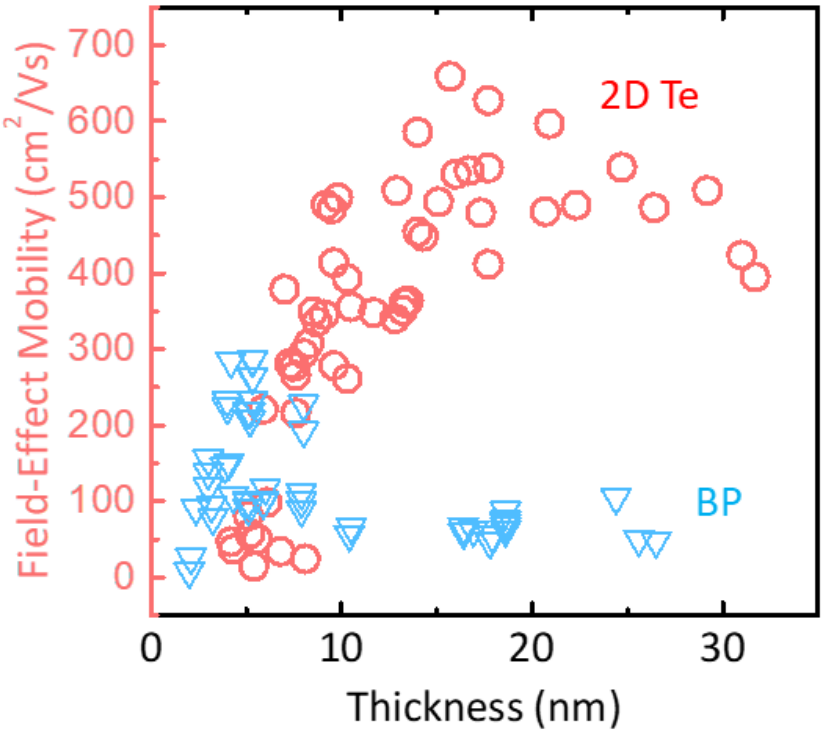

Supplementary Figure 21 | Benchmark comparison of mobility between 2D Te and phosphorene using the same device structure, geometry, and mobility extraction method. The data for phosphorene is from Ref. 13.

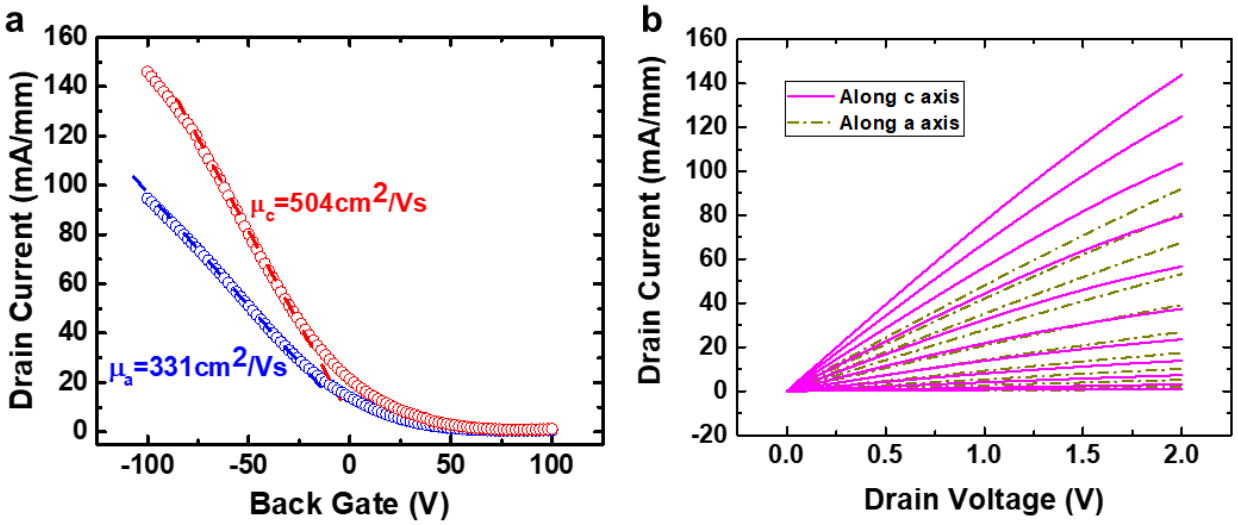

Supplementary Figure 22 | The in-plane anisotropic electrical transport measurement for a 22-nm-thick sample. Here, the c-axis is the [0001] direction, and a-axis is the [$1\bar{2}10$] direction.

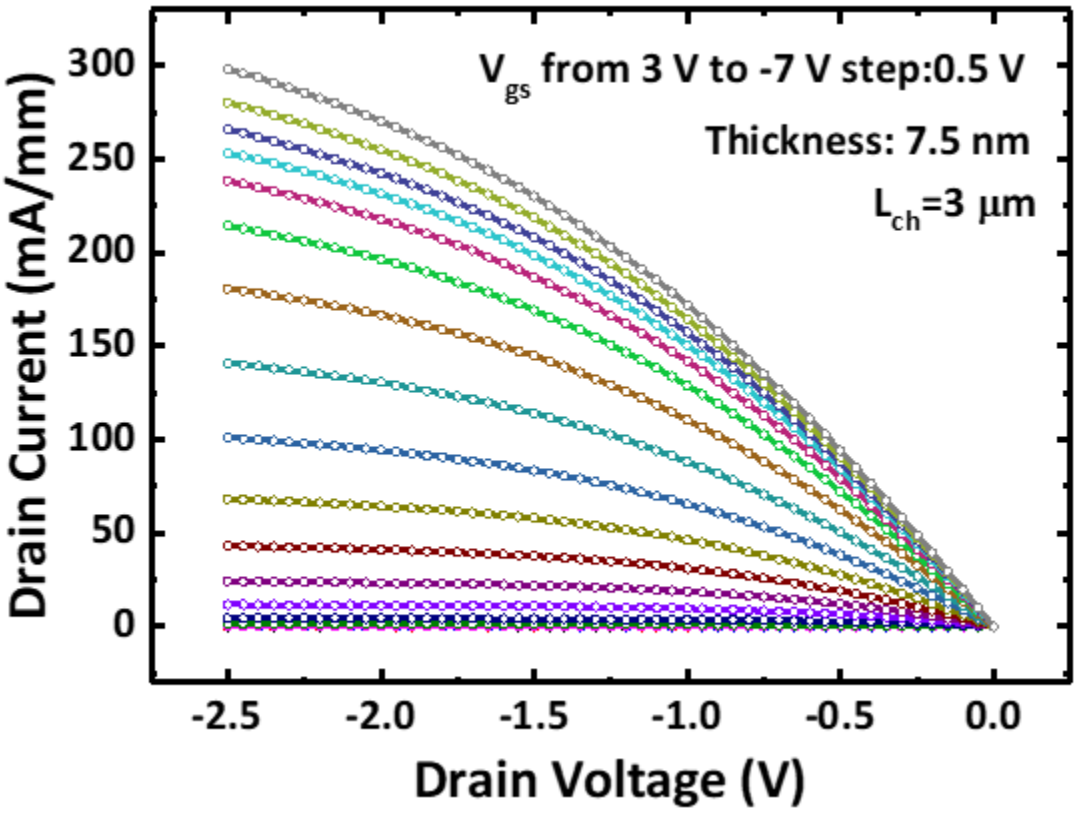

Supplementary Figure 23 | The output curve of the same device shown in Figure 4a. The linear region at small drain bias indicates the contact resistance is negligible.

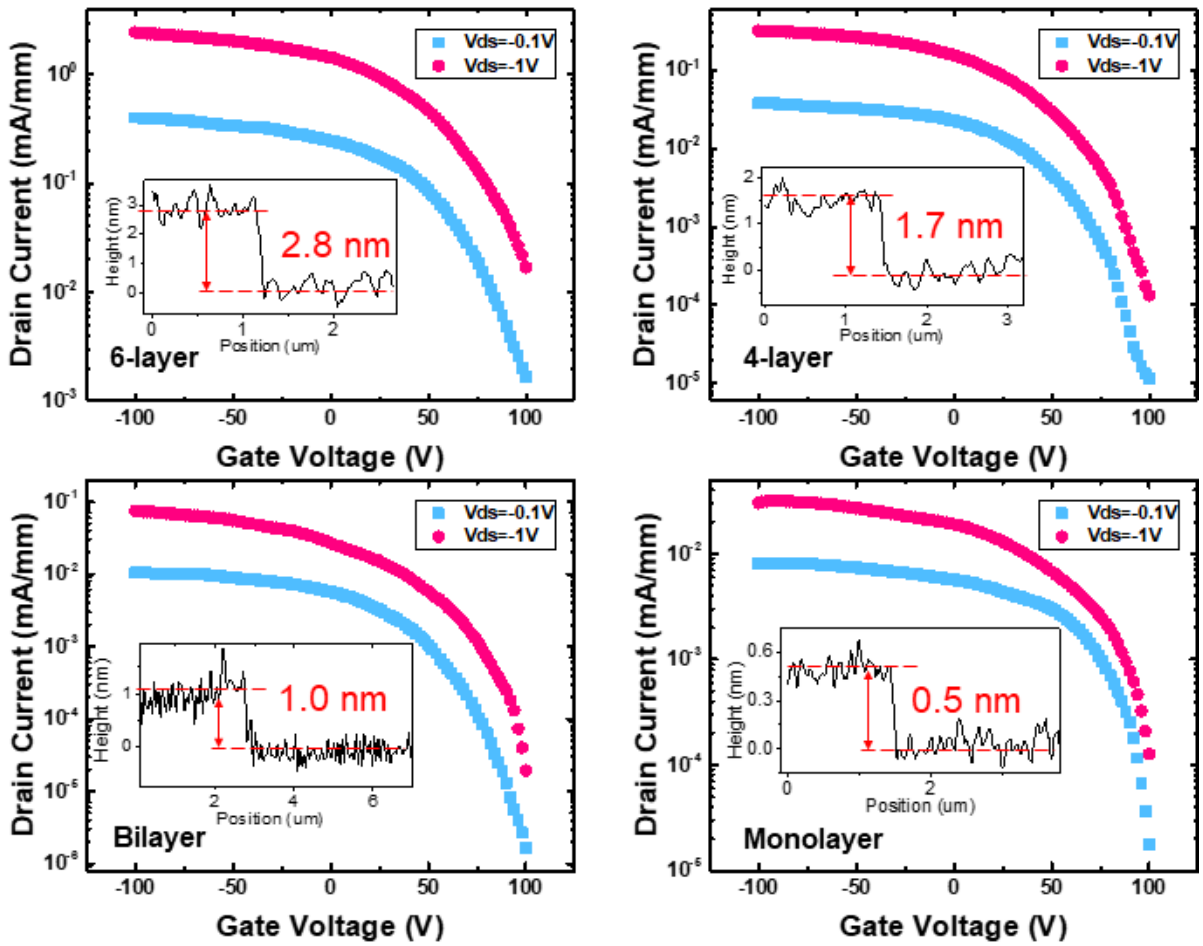

Supplementary Figure 24 | Transfer curves of 2D Te transistors fabricated on 2.8 nm (6L), 1.7 nm (4L), 1.0 nm (2L) and 0.5 nm (1L) flakes, respectively.

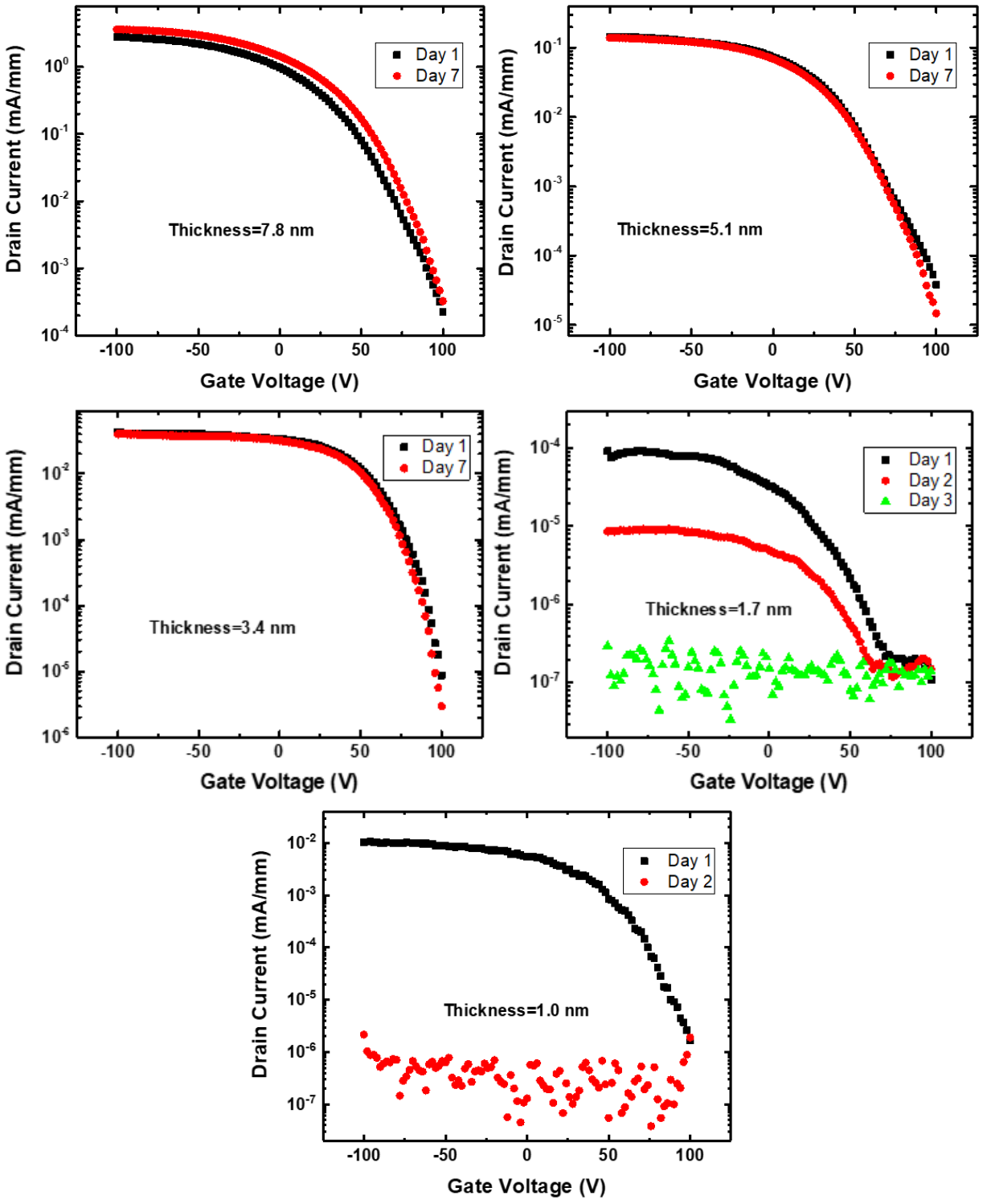

Supplementary Figure 25 | Stability characterization for 2D Te devices with thickness of 7.8 nm, 5.1 nm, 3.4 nm, 1.7 nm, and 1.0 nm measured as-fabricated and after a controlled period without encapsulation in the air.

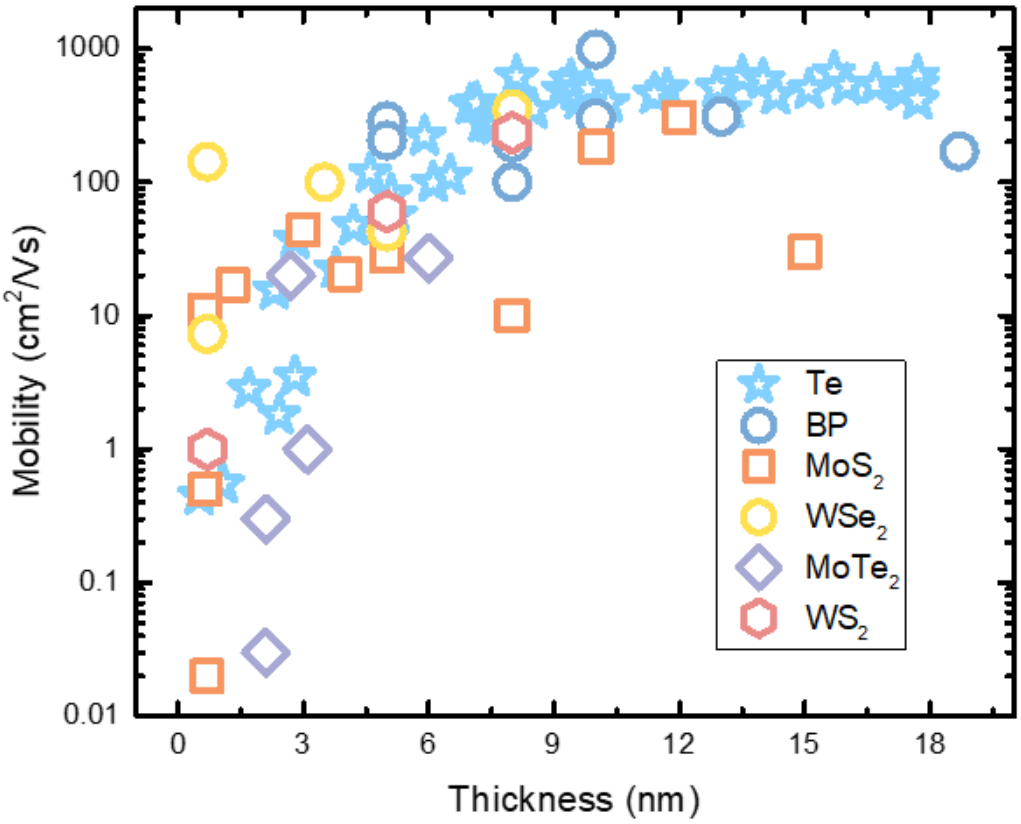

Supplementary Figure 26 | A comparison of mobility values between 2D Te and other 2D semiconductors in different thickness ranges. The data for other 2D materials are extracted from the references listed in the Supplementary Table 1.

Supplementary Table 1: Summary and Comparison of mobility values between 2D Te and other 2D semiconductors in different thickness ranges.[1]

	Reference	Thickness (nm)	Mobility (cm^2/Vs)	Comments
BP	ACS Nano, 2014, 8 (4),4033	5	286	
	Nat. Nanotechnology, 2014, 9, 372	10	984	
		8	197	
		5	55	
	Nat. Commun., 2014, 5, 4458	5	205	
	Nano Lett., 2014, 14 (6),3347	8	100	
	Appl. Phys. Lett., 2014, 104, 103106	10	300	
	ACS Nano, 2014, 8 (10), 10035	18.7	186	Pd contacts
	Nano Lett., 2015, 15(8), 4914	0.55	~1	low-T (10K), h-BN capping
	Nano Lett., 2015, 15 (3), 1883	13	310	
MoS_2	IEEE Electron Device Lett., 2013, 34(10),1328	4	20.4	Molecular Doping
	Proc. Natl. Acad. Sci., 2005, 102(30), 10451	0.65	0.5~3	
	J. Appl. Phys., 2007, 101, 014507	8~40	10~50	
		35	40	
	Appl. Phys. Lett. 102, 142106 (2013)	1.3	17	CVD
	Adv. Mater., 2012, 24(17), 2320	0.7	0.02	CVD
	Nano Lett., 2013, 13 (1), 100	10	184	Scandium Contacts
	ACS Nano, 2013, 7 (6), 5446	15	30	high-k dielectric
	Appl. Phys. Lett., 2014, 104, 093106	0.65	11	Molybdenum contacts
	Appl. Phys. Lett., 2013, 102, 123105 (2013)	12	306	Four-terminal devices
	ACS Nano, 2012, 6 (10), 8563	5	28	

[1] The prototypical 2D Te transistor in this work is merely a demonstration of its exciting electrical properties, whereas most of the state-of-the-art 2D transistors have adopted matured techniques such as doping, dielectric/contact engineering. The summary in **Table 1** shows that 2D Te device has a good all-around figure of merits compared to existing 2D semiconductors. The field-effect mobility of 2D Te has outnumbered almost all *p*-type 2D materials and most of the conventional ultra-thin-body (UTB) semiconductors (Si, GaAs, InAs, etc.). The I_{on} current also surpasses most of its competitors. This is significant in the sense that high-performance PMOS is in principle more challenging to implement than NMOS because holes have lower mobility and larger effective mass than electrons.

	ACS Nano, 2013, 7 (7), 5870	3	44	
WSe_2	Nano Lett. 2012, 12, (7), 3788	0.7	250	NO_2 doping, high-k dielectric
	Nano Lett., 2013, 13 (5), 1983	0.7	142	electrons, Indium contacts
	ACS Nano, 2014, 8 (7), 7180	0.7	30	polymer electrolyte gating
	Sci. Rep., 2015, 5,8979	8	350	
	Nano Lett., 2016, 16 (3), 1896	3.5	200	Nb-doped contacts
	ACS Nano, 2014, 8 (8), 8653	0.7	7.3	CVD
	Nano Lett., 2015, 15 (8), 4928	5	27.4	electrons
		5	42.6	holes
$MoTe_2$	ACS Nano, 2014, 8 (6), 5911	2.7	20	holes
		6	27	electrons
	J. Am. Chem. Soc., 2015, 137 (37), 11892	3.1	1	
	Adv. Mater., 2014, 26(20), 3263	2.1	0.03	holes
		2.1	0.3	electrons
WS_2	ACS Nano, 2014, 8 (8), 8174	0.7	1	
	Nano Lett., 2014, 14 (11), 6275	5	60	Chloride Molecular Doping
	ACS Nano, 2014, 8 (10), 10396	6~8	234	
	Sci. Rep.,2014, 4, 5219	42	16	